# Inversion strength and low cloud amount: A sensitivity study on stratocumulus clouds in DALES

by

**Arno Nederlof**

*Bachelor Thesis*

*Supervisor*
*S.R. de Roode*

*August 2010*

*Clouds, Climate and Air Quality*
*Department of Multi-Scale Physics*
*Faculty of Applied Physics*
*Delft University of Technology*

*"Cloud feedbacks remain the largest source of uncertainty in model based estimates of climate sensitivity"*

IPCC AR4, 2007

**Abstract**

Cloud feedbacks remain the largest source of uncertainty in model based estimates of climate sensitivity. To narrow this uncertainty down it is important to get a better understanding of how stratocumulus clouds evolve over time. In this paper we look at different simulations based on GCSS ASTEX stratocumulus case using DALES v3.1. In these simulations the model was initialized with a solid stratocumulus cloud layer, but in the sensitivity studies the initial values of the humidity and the liquid water potential temperature jumps across the inversion were systematically altered. Results show that the change of the inversion height with time is very dependent on the humidity jump and, secondly the liquid water potential temperature jump. This can be explained by a larger total water flux at the cloud top by turbulent mixing. We were also highly interested in the break up of the stratocumulus cloud. We found that the buoyancy reversal criteria plays a key role. This criterion predicts positive buoyancy fluxes at the clouds top when there is more cooling due to evaporation in relatively dry and warm air, than compensated entrainment warming. Our results show that all clouds that pass the buoyancy reversal line will break up, however DALES just tends to break up clouds as they pass the buoyancy reversal line. From real world observations this should not always be true (B. Stevens, 2003). Lock (2008) introduced a parameter R, which is a measure of the inversion strength. He found that if $R \leq 0.2$ cloud covers of 80% or more seem to occur, while for $R \geq 0.5$ only shallow cumulus appear (with a cloud cover of 20% or less). Our data supports his results, however our spread is bigger than that of Lock's. Finally we found that cases with almost the same initial value of R do not have a similar trajectory of cloud cover or R over time. There was however one set of simulations that did have similar trajectories. This was also the case where the values of R were closest to each other. Further research has to be done, with more grid points and a better way to determine the jumps. Finally runs should be made on other models than DALES to comfirm the results.

# Contents

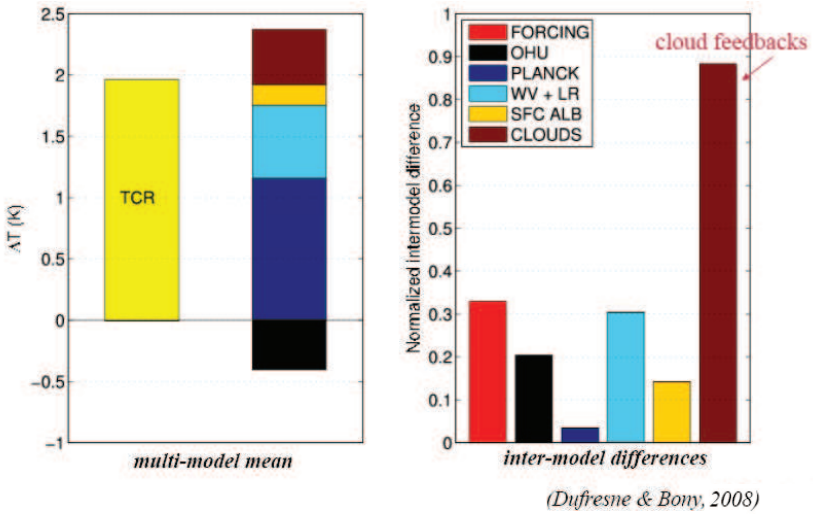


Figure 1: Figure on the left, the change in temperature because of cloud feedback, snow and sea ice feedback, water vapor + lapse rate feedback, basic Planck response and ocean heat uptake. On the right the normalized space standard deviation.

# 1 Introduction

Every day climate becomes a more and more important issue. Politicians are taken precautions to encounter global warming. Many models are used to predict the climate change. But a big uncertainty in climate modeling are clouds. This can be seen in Figure 1. When the temperature on the earth increases, will the global cloud amount increase, block more sunlight and so, cooling the planet? Or will there be less clouds and such that more sunlight is led through, thus increasing the temperature on the Earth even further? The problem for finding the answer to these questions is that clouds are complex. And so the outcome is not easy to predict. One way to find out what is going to happen is to do different simulations of a cloud over time, when changing some parameters in size and see how big the effect is on the cloud. In this bachelor thesis there has been looked at changes of marine stratocumulus clouds over a time period of 40 hours subjected to different external, environmental conditions. Earlier research suggested that the largest contributions to the variance of the LES-derived data for changes in the cloud-top jump of the total water mixing ratio ($\Delta q_t$) and the net radiative flux (Chlond and Wolkau 1999). In this thesis the humidity jump is also varied, together with changes of the liquid water potential temperature jump across the inversion. To simulate the cloud the Dutch Atmospheric Large Eddy Simulation (DALES) was used. Finally the data will be compared to a paper posted by Lock in 2008. He looked at the buoyancy reversal criteria, and how it effects the break up of clouds.

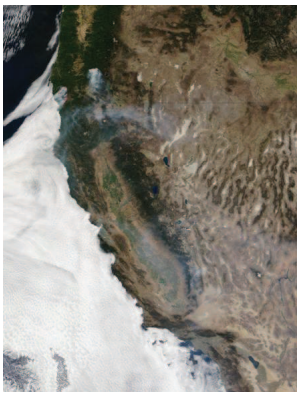

Figure 2: A stratocumulus cloud off the coast of Oregon/California. The image was acquired with MODIS

# 2 Theory

Stratocumuli usually occur in large sheets. They belong to the low level clouds, which means they have a low altitude and so are easily influenced by the conditions on the earth's surface. If the cloud does not get a continuous supply of moisture it will dissolve. That is why stratocumulus clouds are mostly observed above the sea (see Figure 2).

## 2.1 The potential temperature

Before going into more detail on the stratocumulus cloud, it is important that some parameters are introduced. One of them is the potential temperature $\theta$. If a parcel of fluid is adiabatically brought from pressure $p$ to a standard reference pressure $p_0$ the temperature that the parcel would acquire is the potential temperature. It can be derived from the second law of thermodynamics:

$$Tds = du + pdv \geq 0 \tag{1}$$

Here $T$ is the temperature, $s$ the specific entropy, $u$ the internal energy, $p$ the pressure and $v$ the specific volume. This equation can be rewritten using the specific enthalpy h:

$$h = u + pv \rightarrow dh = d\left(u + pv\right) = du + pdv + vdp \tag{2}$$

Filling this back in equation 1 we obtain:

$$Tds = dh - vdp \tag{3}$$

The enthalpy can be written in terms of specific heat at constant pressure $c_p$:

$$c_p = \left(\frac{\partial h}{\partial T}\right)_p \tag{4}$$

Because the pressure never exceeds 1050hPa it can be assumed that air behaves like an ideal gas. The other term $vdp$ can be rewritten using the ideal gas law:

$$pv = R_d T \tag{5}$$

With $\rho$ the density (in this case of air) and $R_d$ the specific gas constant of dry air. Now filling everything back into equation (3) and divide the whole equation by $T$:

$$ds = c_p \frac{dT}{T} - R_d \frac{dp}{p} \tag{6}$$

For an isotropic process $ds = 0$ so:

$$\frac{dT}{T} = \frac{R_d}{c_p} \frac{dp}{p} \tag{7}$$

Integrating this from a reference point $(p_0, \theta)$:

$$\int_\theta^T \frac{1}{T}\, dT = \frac{R_d}{c_p} \int_{p_0}^p \frac{1}{p}\, dp \rightarrow \frac{T}{\theta} = \left(\frac{p}{p_0}\right)^{\frac{R_d}{c_p}} \rightarrow \theta = \frac{T}{\Pi} \tag{8}$$

Now we have obtained an expression for the potential temperature. $\Pi$ is called Exner function given by:

$$\Pi = \left(\frac{p}{p_0}\right)^{\frac{R_d}{c_p}} \tag{9}$$

But this is for dry air. In real life, outside, the air is never dry, it's humid. The total humidity is given by:

$$q_t = q_v + q_l \tag{10}$$

Here $q_t$ is the total humidity, $q_v$ is the vapor water content and $q_l$ the liquid water content. In order to make the formulas above applicable again the specific gas constant $R_d$ has to change into the specific gas constant for moist air. But it is more convenient to keep working with $R_d$. So instead of changing the constant $R_d$, the temperature of equation (8) is changed into $T_v$, defined as the temperature a dry parcel of air would have if it's pressure were equal to those of moist air. $T_v$ is given in Stull (1988):

$$T_v = \left(1 + \epsilon_I q_t - \frac{q_l}{\epsilon}\right) T \tag{11}$$

Where $\epsilon = \frac{R_d}{R_v} \approx 0.62$ and $\epsilon_I = \frac{1}{\epsilon} - 1 \approx 0.608$. This gives a virtual potential temperature $\theta_v$ given by

$$\theta_v = \frac{T_v}{\Pi} \tag{12}$$

When clouds form, condensed water releases heat into the surrounding air, subsequently warming it. To compensate for this the liquid water potential temperature is introduced, given by $\theta_l$.

$$\theta_l = \theta - \frac{L}{c_p} q_l \tag{13}$$

With L the latent heat of water. Now equations (11) and (12) can be used to derive a new expression for $\theta_v$.

$$\theta_v = \left(1 + \epsilon_I q_t - \frac{q_l}{\epsilon}\right) \theta \tag{14}$$

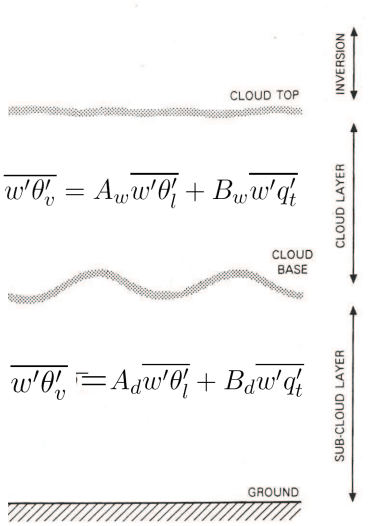


Figure 3: The build up of a stratocumulus cloud

Now we write $q_t$ as:

$$q_t = q_s + q_l \tag{15}$$

Where $q_s$ is the saturation specific humidity. This is only possible if supersaturation is negligible in the boundary layers of the stratocumulus (see e.g. Albrecht et al., 1995, fig. 9). Now if Reynolds-averaging is used (splitting it up in a average part and its fluctuations).

$$\Psi\left(x,y,z,t\right) = \overline{\Psi}\left(x,y,z\right) + \Psi'\left(x,y,z,t\right) \tag{16}$$

With $\Psi \,\epsilon\, \{q_s, q_l, \theta_v, \theta, u, v, w\}$. The overbar represents the spatial average and the prime represents the fluctuation. Applying this Reynolds-averaging on equation (14) we gain:

$$\theta'_v = \theta_v - \overline{\theta_v} = \left(\epsilon_I q'_s - q'_l\right)\overline{\theta} + \left(1 + \epsilon_I\overline{q_s} - \overline{q_l}\right)\theta' \tag{17}$$

Multiplying this equation with the vertical velocity equation $w'$ and taking the average:

$$\overline{w'\theta'_v} = \left(\epsilon_I\overline{w'q'_s} - \overline{w'q'_l}\right)\overline{\theta} + \left(1 + \epsilon_I\overline{q_s} - \overline{q_l}\right)\overline{w'\theta'} \tag{18}$$

This is an expression for the virtual potential temperature flux which is linked to buoyancy.

## 2.2 The build up of a stratocumulus cloud

A marine stratocumulus cloud can be divided into 6 regions. The sub-cloud layer, the cloud base, the cloud layer, cloud top, the inversion and the free atmosphere, see Figure 3.

### 2.2.1 The sub-cloud layer

If we start from the sea surface and go up, we first arrive in the sub-cloud layer. Here the air is unsaturated and so all the water in the air exist of cloud vapor ($q_l \approx 0 \rightarrow q_t = q_v$). This reduces equation (18) to:

$$\overline{w'\theta'_v} = \epsilon_I \overline{w'q'_t}\overline{\theta} + (1 + \epsilon_I \overline{q_t})\,\overline{w'\theta'} \tag{19}$$

Furthermore the potential liquid water temperature flux is now equal to the potential temperature flux:

$$\overline{w'\theta'_l} = \overline{w'\theta'} - \frac{L}{c_p}\overline{w'q'_l} = \overline{w'\theta'} \tag{20}$$

Thus equation (19) becomes:

$$\overline{w'\theta'_v} = \epsilon_I \overline{w'q'_t}\overline{\theta} + (1 + \epsilon_I \overline{q_v})\,\overline{w'\theta'_l} = A_d \overline{w'\theta'_l} + B_d \overline{w'q'_t} \tag{21}$$

Where $A_d \approx 1.01$ and $B_d \approx 170$ for dry convection.

### 2.2.2 The cloud base and cloud layer

The transition from the sub-cloud layer to the cloud base is poorly defined. This is because there is no stability and there is a large variation in cloud base height. Inside the cloud the air is well mixed. The total humidity now exists again of liquid and vapor water. Using equation (15).

$$\epsilon_I q_s - q_l = (1 + \epsilon_I) q_s - q_t = \frac{q_s}{\epsilon} - q_t \tag{22}$$

Now equation (18) becomes:

$$\overline{w'\theta'_v} = \left(\frac{\overline{w'q'_s}}{\epsilon} - \overline{w'q'_t}\right)\overline{\theta} + \left(1 + \frac{\overline{q_s}}{\epsilon} - \overline{q_t}\right)\overline{w'\theta'} \tag{23}$$

Using the Clausius-Clapeyron equation a expression for $q'_s$ can be derived

$$\frac{dq_s}{dT} = \frac{L q_s}{R_v T^2} \tag{24}$$

Now because $q'_s$ is a fluctuation we can say $dq_s = q'_s$ and $dT = T'$.

$$q'_s = \frac{dq_s}{dT} T' \rightarrow \overline{w'q'_s} = \frac{dq_s}{dT}\overline{w'T'} \approx \frac{dq_s}{dT}\overline{w'\theta'} \tag{25}$$

Substituting this back into equation (23)

$$\overline{w'\theta'_v} = -\overline{\theta}\overline{w'q'_t} + \left(1 + \frac{\overline{q_s}}{\epsilon} - \overline{q_t} + \frac{\overline{\theta}}{\epsilon}\frac{dq_s}{dT}\right)\overline{w'\theta'} \tag{26}$$

Now again using equation (20), but now with $q_l$ not equal to zero.

$$\overline{w'\theta'_v} = \overline{w'\theta'_l}\left(1 + \frac{\overline{q_s}}{\epsilon} - \overline{q_t} + \frac{\overline{\theta}}{\epsilon}\frac{dq_s}{dT}\right) + \overline{w'q'_l}\left(\frac{L}{c_p}\right)\left(1 + \frac{\overline{q_s}}{\epsilon} - \overline{q_t} + \frac{\overline{\theta}}{\epsilon}\frac{dq_s}{dT}\right) - \overline{\theta}\overline{w'q'_t} \tag{27}$$

The last thing that has to be done is substituting out $\overline{w'q_l'}$. Therefore we write:

$$\begin{aligned}\overline{w'q_l'} &= \overline{w'q_t'} - \overline{w'q_s'} = \overline{w'q_t'} - \frac{dq_s}{dT}\overline{w'\theta'} \\ &= \overline{w'q_t'} - \frac{dq_s}{dT}\left(\overline{w'\theta_l'} + \frac{L}{c_p}\overline{w'q_l'}\right)\end{aligned} \tag{28}$$

So:

$$\overline{w'q_l'} = \frac{\overline{w'q_t'}}{1 + \frac{L}{c_p}\left(\frac{dq_s}{dT}\right)} - \frac{\overline{w'\theta_l'}\left(\frac{dq_s}{dT}\right)}{1 + \frac{L}{c_p}\left(\frac{dq_s}{dT}\right)} \tag{29}$$

Substituting this back into equation (27) we gain.

$$\overline{w'\theta_v'} = A_w\overline{w'\theta_l'} + B_w\overline{w'q_t'} \tag{30}$$

With coefficients:

$$A_w = \frac{1 + \frac{\overline{q_s}}{\epsilon} - \overline{q_t} + \frac{\overline{\theta}}{\epsilon}\frac{dq_s}{dT}}{1 + \frac{L}{c_p}\left(\frac{dq_s}{dT}\right)} \approx 0.5 \tag{31}$$

and

$$B_w = A_w\frac{L}{c_p} - \overline{\theta} \approx 1100 \tag{32}$$

If we now look at the profiles of $\overline{w'\theta_l'}$ and $\overline{w'q_t'}$ we can see that that $\overline{w'\theta_v'}$ is really built up like this (See Figure 4). In the subcloud layer $\overline{w'\theta_l'}$ dominates the $\theta_v$ flux, because (even with factor $B_d \approx 170$) $\overline{w'q_t}$ is still relatively small compared to $\overline{w'\theta_l'}$. In the cloud $\overline{w'q_t}$ starts to dominate, because now with factor $B_w \approx 1100$ it is bigger than $\overline{w'\theta_l'}$.

### 2.2.3 Cloud top, inversion and the free atmosphere

If we go further up we will reach the cloud top, inversion and finally the free atmosphere. In the free atmosphere the region is relatively warm and dry, compared to the cloud top, the air is stable and there is little turbulence. The inversion resides between the cloud top and the free atmosphere. The temperature profiles show a strong vertical gradient, because of the big difference between the cold wet air from the cloud and the relatively dry warm air above. This strong temperature gradient makes the air stable. In this part the local perturbations are strongly damped, so the cloud is fairly flat. This strong gradient can be seen back in the profiles of $q_t$, $\theta_l$ and their fluxes (see Figures 4 and 5). The jumps they make in the inversion are indicated as $\Delta q_t$ and $\Delta\theta_v$

## 2.3 Time dependency

All objects radiate energy, so also the liquid water droplets inside the cloud. Inside the cloud the net longwave radiation is zero, but on the edges it isn't. Because the Earth's surface is more hot than the cloud. The cloud is warmed from underneath. At the cloud top more radiation is emitted than absorbed, the radiation is in the infrared regime and therefore called cloud-top longwave radiative cooling. The air

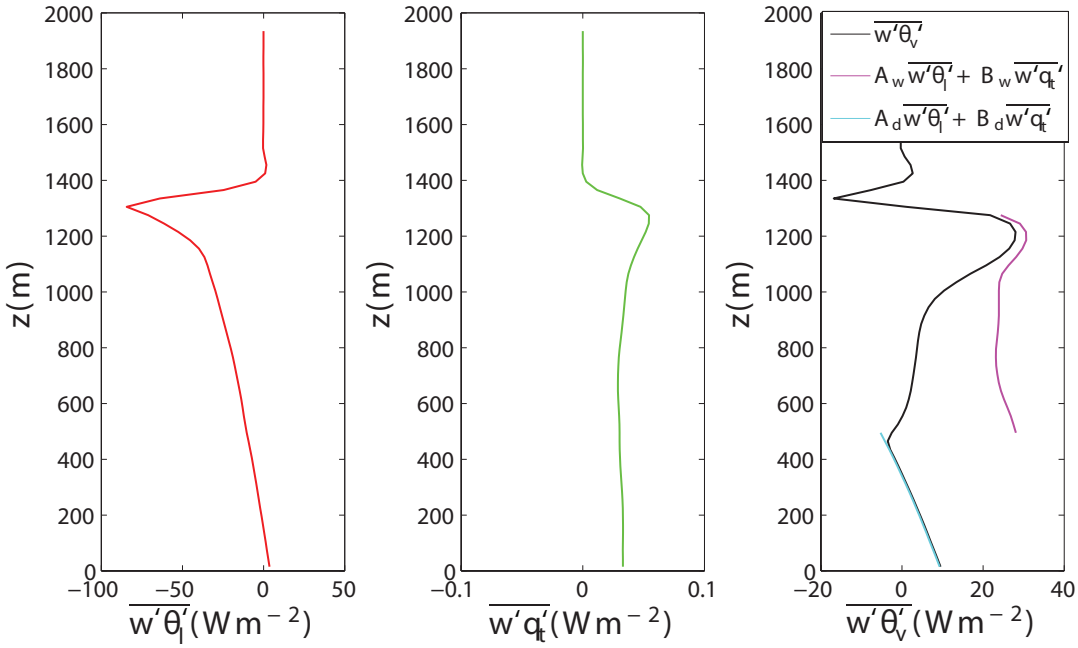


Figure 4: A profile for the vertical fluxes $\overline{w'\theta_l'}$, $\overline{w'q_t'}$ and $\overline{w'\theta_l'}$ multiplied with $\rho c_p$

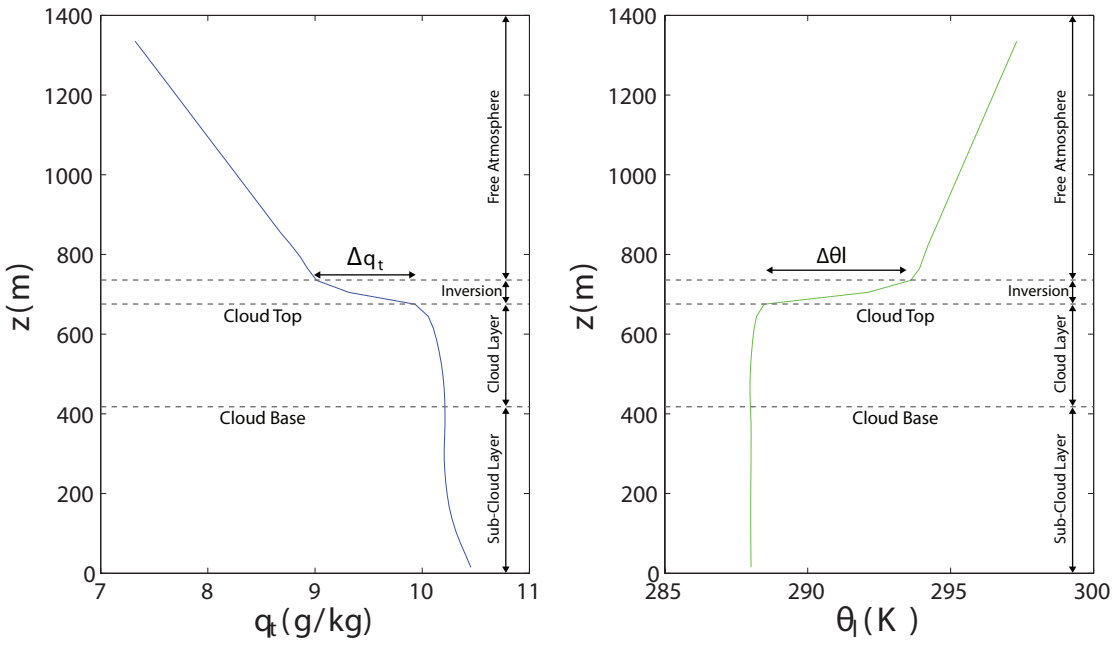


Figure 5: A $q_t$ and $\theta_l$ profile

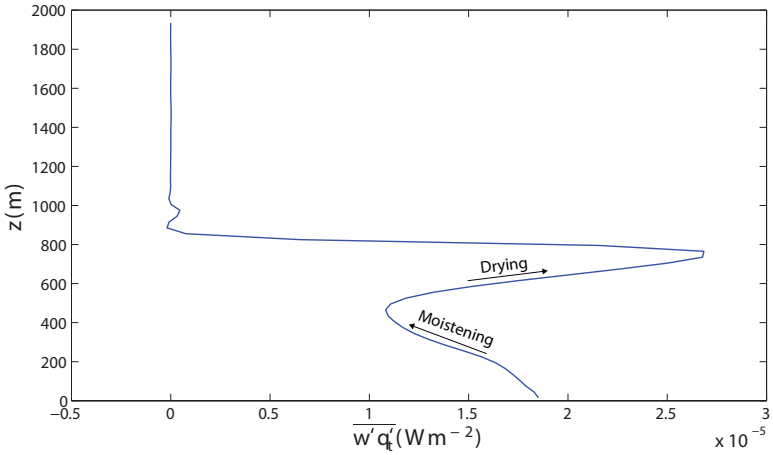


Figure 6: A $\overline{w'q'_t}$ profile. With moistening at the base and drying at the top

parcels at the top cool and start to sink down, creating downdrafts, which on their turn create turbulence. This turbulence enables moisture from the bottom to reach the cloud top, which thickens the cloud. Turbulence also causes air from above the cloud to enter to cloud. This is the entrainment. Because the air above the cloud is warmer and dryer the air just below the inversion warms and dries out. During the day the cloud-top longwave radiative cooling is compensated by solar, or shortwave radiative warming. This will generate less turbulence, and so less entrainment. This will cause the cloud to thin during the day. The rate of change of $q_t$ and $\theta_l$ can be defined as:

$$\frac{d\overline{q_t}}{dt} = -\frac{\partial \overline{w'q'_t}}{\partial z} \tag{33}$$

and

$$\frac{d\overline{\theta_l}}{dt} = -\frac{\partial \overline{w'\theta'_l}}{\partial z} - \frac{\partial F}{\partial z} \tag{34}$$

Here F is the net radiation flux,

$$F = \frac{1}{\overline{\rho} c_p} \left(F_L \uparrow - F_L \downarrow + F_S \uparrow - F_S \downarrow\right) \tag{35}$$

Here $F_L$ is the longwave radiation and $F_S$ the shortwave radiation. In the subcloud layer only the flux divergence within the cloud is of importance. The arrows indicate the direction of the radiation. If we take the changes in height in equations (33) and (34) between the ground and the inversion height we gain:

$$\frac{d\overline{q_t}}{dt} = \frac{\overline{w'q'_{t0}} - \overline{w'q'_{t_{z_i}}}}{z_i} \tag{36}$$

and

$$\frac{d\overline{\theta_l}}{dt} = \frac{\overline{w'\theta'_{l0}} - \overline{w'\theta'_{l_{z_i}}}}{z_i} + \frac{F_0 - F_{z_i}}{z_i} \tag{37}$$

Here $z_i$ indicates the inversion height and the subscript 0 indicates sea level ($z = 0$). The effect of moistening and drying have been made more clear in Figure 6. For an infinitesimally thin inversion layer

the flux at the boundary top can be expressed as.

$$\begin{aligned}\overline{w'q'_t}_{z_i} &= -w_e\Delta\overline{q_t} \\ \overline{w'\theta'_l}_{z_i} &= -w_e\Delta\overline{\theta_l}\end{aligned} \tag{38}$$

Here $w_e$ is the entrainment velocity. Putting this back into equation (36) and (37) we obtain.

$$\frac{d\overline{q_t}}{dt} = \frac{\overline{w'q'_{t0}} + w_e\Delta\overline{q_t}}{z_i} \tag{39}$$

and

$$\frac{d\overline{\theta_l}}{dt} = \frac{\overline{w'\theta'_{l0}} + w_e\Delta\overline{\theta_l}}{z_i} \tag{40}$$

Equation (39) tells us that if there is an increasing entrainment, the liquid water content will decrease (keep in mind that $\Delta q_t$ is negative, see Figure 5). The entrainment of dry air at the top is an effect imposed by radiation. In general the entrainment is a function of:

$$w_e = f\left(\Delta q_t, \Delta\theta_l, \overline{w'q'_t|_0}, \overline{w\theta'_l|_0}, DF_R, z_b, z_t\right) \tag{41}$$

Here $z_b$ is the cloud base, $z_t$ is the cloud top, $DF_R$ is a the change in radiation between the inversion and the ground.

$$DF_R = F_R|_{zi} - F_R|_0 \tag{42}$$

A simple version for the entrainment rate is introduced by Moeng (CM) given by

$$w_e = \frac{0.2\rho_0 c_p\overline{w'\theta'_l}|_0 + DF_R\left[2.5 - 2e^{-b_m\sqrt{W_p}}\right]}{\rho_0 c_p\Delta\theta_l} \tag{43}$$

Here $\rho_0$ is a reference density of air and $b_m$ a constant with value 0.9. In equation (43), $W_p$ is the liquid water path. The liquid water path is given by

$$W_p = \int_{z_b}^{z_t}\rho_{air}q_l\,dz \tag{44}$$

Here $\rho_{air}$ the density of air. Normally $\rho_{air}$ also depends on the height ($z$) but for convenience this is chosen to be a constant $\rho_{air} = 1.14kg\ m^{-3}$ . In this thesis the trapezoidal method is used to calculate this integral. A change in the inversion height is also influenced by the entrainment.

$$\frac{dz_i}{dt} = w_e + \overline{w} \tag{45}$$

Here $\overline{w}$ is the large-scale velocity, which is typically negative in the stratocumulus boundary layers due to a large scale divergence of the mean horizontal winds. This equation in general describes the entrainment versus the subsidence. Depending on which factor is bigger the cloud top will fall or rise.

## 2.4 From stratocumulus to cumulus

An important part is to determine when a stratocumulus cloud breaks up into a cumulus. There are different ways of doing this. We start of with the most important one: Buoyancy reversal.

### 2.4.1 Buoyancy reversal

The buoyancy flux is the dominant production term in of the turbulent kinetic energy(TKE) in the boundary layer. The TKE per unit mass is given by

$$\frac{TKE}{m} = \frac{1}{2}\left(\overline{u'^2} + \overline{v'^2} + \overline{w'^2}\right) = \overline{e} \tag{46}$$

With $u$ the speed in the $x$ direction, $v$ the speed in the $y$ direction and $w$ the speed in the z-direction. If we use the index notation:

$$\overline{u_i'^2} = \overline{u'^2} + \overline{v'^2} + \overline{w'^2} \tag{47}$$

The TKE budget equation can be written as follows

$$\begin{array}{ccccccccccccc} \frac{\partial \overline{e}}{\partial t} & + & \overline{U_j}\frac{\partial \overline{e}}{\partial x_j} & = & \delta_{i3}\frac{g}{\overline{\theta_v}}\left(\overline{u_i'\theta_v'}\right) & - & \overline{u_i'u_j'}\frac{\partial \overline{U_i}}{\partial x_j} & - & \frac{\partial \overline{u_j' e}}{\partial x_j} & - & \frac{1}{\rho}\frac{\partial\left(\overline{u_i' p'}\right)}{\partial x_i} & - & \epsilon \\ I & & II & & III & & IV & & V & & VI & & VII \end{array} \tag{48}$$

Here

**Term I** storage or tendency of TKE

**Term II** advection of TKE by mean wind

**Term III** buoyant production or consumption term. Mind the $\delta_{i3}$ which indicates that only the vertical velocity is used ($\overline{u_i'\theta_v'} = \overline{w'\theta_v'}$). And $g$ is the gravity constant.

**Term IV** mechanical or shear production/loss term.

**Term V** turbulent transport of TKE

**Term VI** pressure correlation term

**Term VII** viscous dissipation of TKE

According to equation (30) the buoyancy flux at the top of the cloud can be rewritten into:

$$\overline{w'\theta_v'}_{z_i} = -w_e\left(A_w\Delta\overline{\theta_l} + B_w\Delta\overline{q_t}\right) \tag{49}$$

If now warm and dry air from above the inversion is entrained and mixed into the cloud layer, the parcel will cool down due to evaporation of cloud droplets. This cooling can more than compensate the warming due to entrainment. The parcel will become negative buoyant with respect to its environment. This is called buoyancy reversal and occurs if:

$$\Delta\overline{\theta_l} < -\frac{B_w}{A_w}\Delta\overline{q_t} \tag{50}$$

Here, if we take $\Delta q_t$ in g/kg then $\frac{B_w}{A_w} = \frac{1100}{0.5*1000} = 2.2$. The negatively buoyant parcels will start to sink, because they are more heavy than their environment. This will create turbulence, which will lead

to more entrainment. Which will lead to the break up of the cloud (see equations (39) and (45)). In Lock (2008) a parameter $R$ is introduced, given by

$$R = \frac{\Delta\overline{\theta_e}}{L/c_p\Delta\overline{q_t}} \tag{51}$$

According to Lock this parameter gives some measure of the buoyancy of the parcels of air formed from mixtures of cloudy air and so determines the cloud cover of the cloud. This $R$ has some offset compared to the buoyancy reversal criteria. In equation (51), the equivalent potential temperature is introduced ($\theta_e$). The equivalent potential temperature includes the additional heating caused by release of latent heat when air condenses and is approximately given by:

$$\theta_e \approx \theta exp\left(\frac{Lq_v}{c_pT}\right) \tag{52}$$

The exponential function here is sufficiently small so this can be rewritten to:

$$\theta_e \approx \theta + \frac{Lq_v}{c_p} \tag{53}$$

Now combining this with equation (13) we gain:

$$\theta_e \approx \theta_l + \frac{L}{c_p}q_t \tag{54}$$

Placing this back into equation (51):

$$R = \frac{\Delta\overline{\theta_l} + \frac{L}{c_p}\Delta q_t}{\frac{L}{c_p}\Delta\overline{q_t}} \tag{55}$$

Now this can be used to write equation (51) in the same form as the buoyancy reversal criterion only now for when R becomes bigger than 0.

$$\Delta\overline{\theta_l} < -\frac{L}{c_p}\Delta\overline{q_t} \tag{56}$$

This is almost the same as equation (50) except the factor is different. In equation (50) the factor was $\frac{B_w}{A_w} \approx 2.2$ for $\Delta\overline{q_t}$ in g/kg, here the factor is $\frac{L}{c_p}$ which is 2.5, if we take $\Delta\overline{q_t}$ in g/kg. To be able to compare the results with Lock, in this thesis the R criterion is also used. Lock came to the conclusion that for $R \leq 0.2$ cloud covers of 80% or more seem to occur, while for $R \geq 0.5$ only shallow cumulus appear (with a cloud cover of 20% or less). This can be seen in Figure 7.

### 2.4.2 Saturation vapor specific humidity

Now we are going to at the saturation vapor specific humidity ($q_{sat}$). Which is given by:

$$q_{sat} = \frac{r_{sat}}{1 + r_{sat}} \tag{57}$$

Where $r_{sat}$ is the saturation mixing ratio which depends on the saturation vapor pressure ($e_{sat}$ ):

$$r_{sat} = \frac{R_d}{R_v}\frac{e_{sat}}{p - e_{sat}}; \tag{58}$$

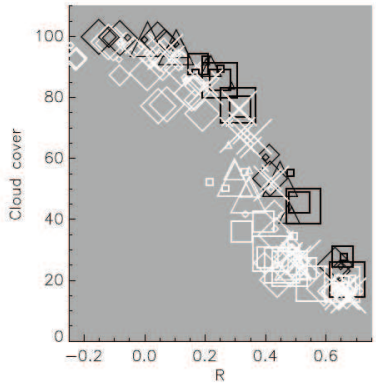


Figure 7: Lock's findings on the cloud cover versus parameter R

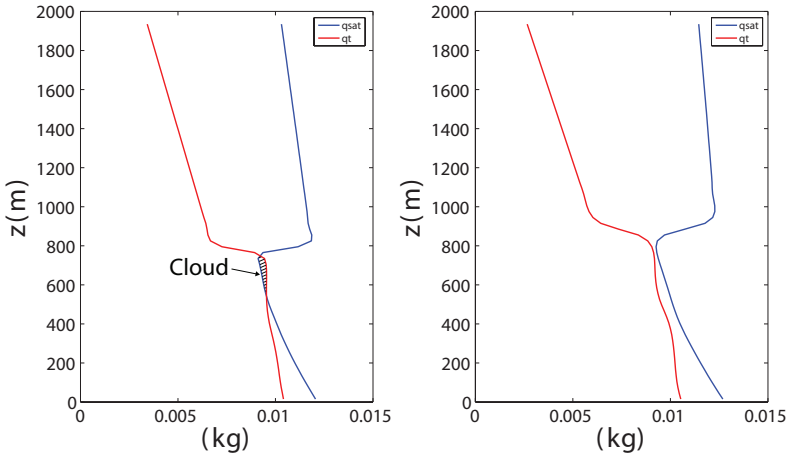


Figure 8: The $q_{sat}$ and $q_t$ profiles. With on the left overlap, so there is cloud and on the right no overlap and so no cloud, however, because these values are horizontal mean values at some places $q_{sat} \leq q_t$ and therefore cumulus still can be present.

The saturation vapor pressure is given by:

$$e_{sat} = 610.78e^{\frac{17.2694T-273.16}{T-35.86}} \tag{59}$$

Now if the $\overline{q_{sat}}$ profile and the $\overline{q_t}$ profile have overlap (see Figure 8) then in that part there is a cloud, however, if they do not overlap it does not have to mean that there is no cloud. Because these values are horizontal mean values at some places $q_{sat} \leq q_t$ and therefore cumulus still can be present.

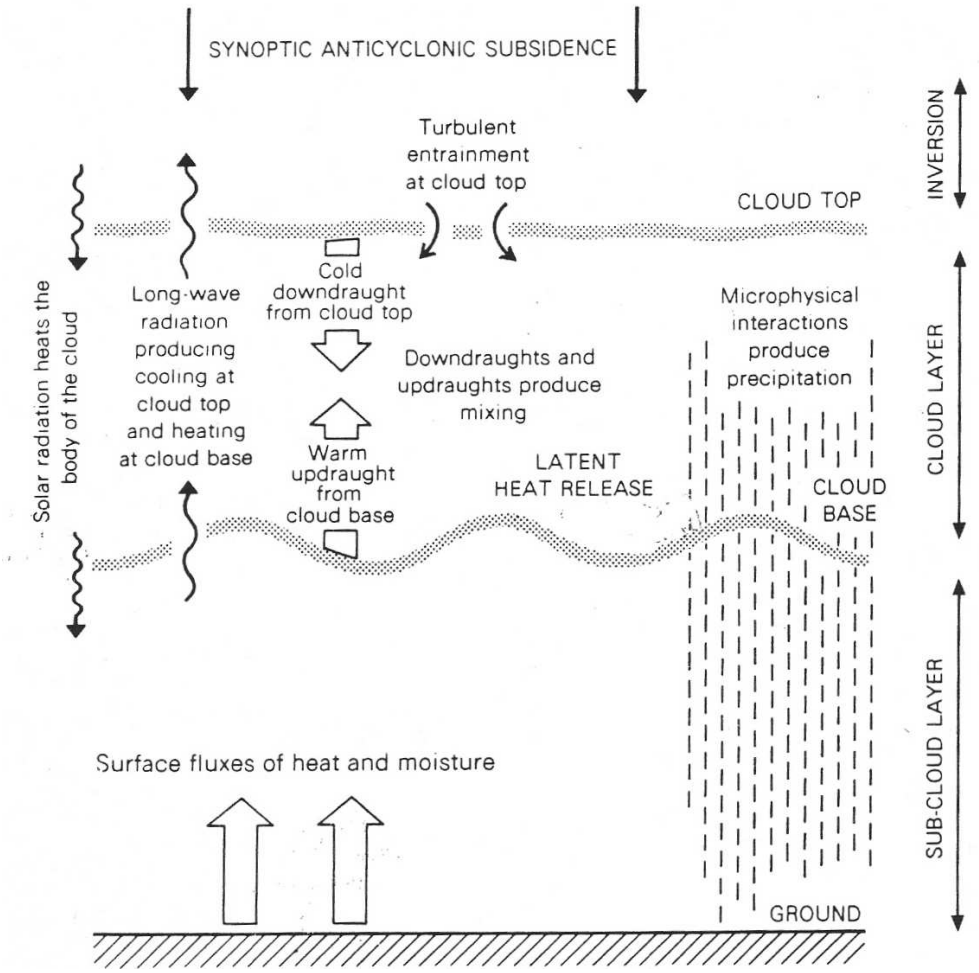


Figure 9: Summary of physical processes important to the development of stratocumulus (S. Nicholls, 1986)

## 2.5 Summary

The stratocumulus cloud is a low level cloud with a high cloud cover percentage. In Figure 9 a summary is given of most of the mechanisms that have an effect on the cloud. An important mechanism for break up of the cloud is the radiative heating and cooling and the turbulence that is caused by it. The TKE budget with a coordinate system aligned with the mean wind is:

$$\underset{I}{\frac{\partial \overline{e}}{\partial t}} = \underset{III}{\frac{g}{\overline{\theta_v}}\left(\overline{w'\theta_v'}\right)} - \underset{IV}{\overline{u'w'}\frac{\partial \overline{U}}{\partial z}} - \underset{V}{\frac{\partial \overline{w'e}}{\partial z}} - \underset{VI}{\frac{1}{\rho}\frac{\partial\left(\overline{w'p'}\right)}{\partial z}} - \underset{VII}{\epsilon} \tag{60}$$

The mean advection term vanishes because of the cyclic horizontal boundary condition. Term III in this equation is called the buoyant production or consumption term. This term can be positive or negative and so can have a damping or increasing effect on the TKE. If $\Delta\theta_l < -\frac{B_w}{A_w}\Delta q_t$ then term III has a increasing effect on the TKE (For a derivation see equation (48) till (50)). This means more entrainment of dry and warm air, more turbulence, which will lead to the break up of the cloud.

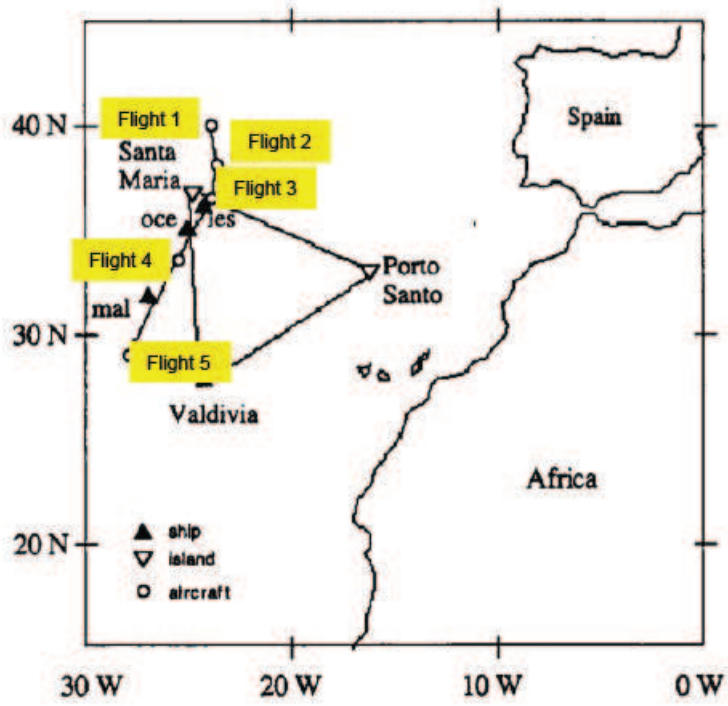


Figure 10: The five flights of ASTEX First Lagrangian in 1992 (de Roode and van der Dussen,2010)

# 3 Experimental setup

## 3.1 Setup

In this Bachelor end project the Dutch Atmospheric Large Eddy Simulation(DALES) model was used. There were no changes made to this model. Instead, just the initialization for DALES has been altered. In this chapter this initialization is discussed. The initialization is based on the GCSS ASTEX stratocumulus observations. The Atlantic Stratocumulus Transition Experiment (ASTEX) were five flights that took place from 1 June through 25 June 1992 off the northwest coast of Africa near the Azores, Madeira and Canary Island groups. The experiment area extended from 10N to 45N latitude and 40W to 10E longitude, see Figure 10. A schematic of the flights can be found in Figure 11. Because they flew from north to south the sea surface temperature increased with 4.3 K. This is also included in the model used here. In the initialization a slight alteration is made between $662.5 < z < 712.5\ m$. The idealized profiles of $q_t$, $\theta_l$ and the velocities in the $x$ and $y$-directions are as follows

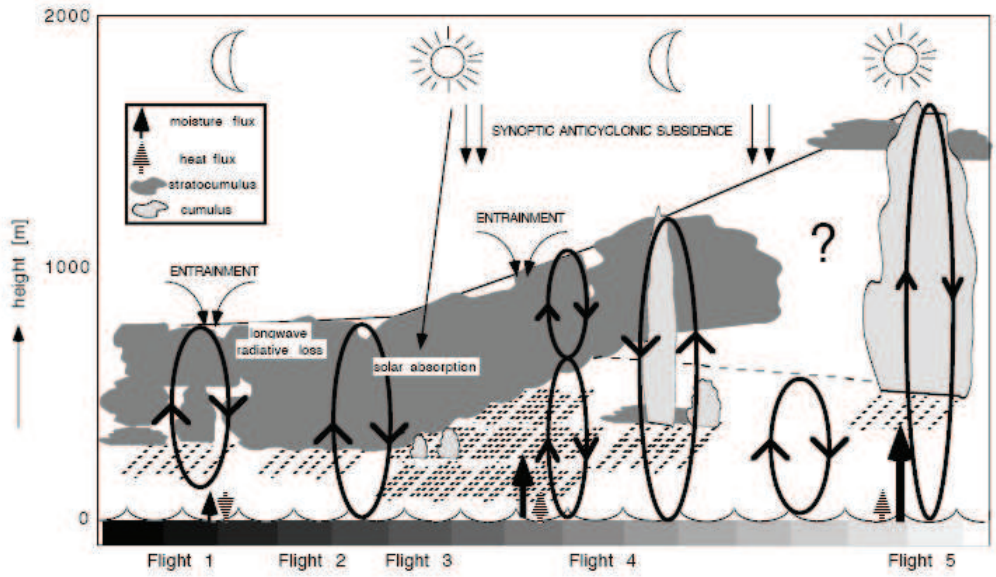


Figure 11: A schematic of the five flights of ASTEX. The gray bar on the bottom indicates the increasing sea water temperature (de Roode and van der Dussen,2010)

$$
\begin{aligned}
&0 < z < 662.5\text{m} && \begin{cases} \overline{u} = -0.7 & m\ s^{-1} \\ \overline{v} = -10.0 & m\ s^{-1} \\ \overline{\theta_l} = 288 & K \\ \overline{q_t} = 10.2 & g\ kg^{-1} \end{cases} \\
&662.5 < z < 712.5\text{m} && \begin{cases} \overline{u} = -0.7 - 0.026\,(z - 662.5) & m\ s^{-1} \\ \overline{v} = -10.0 & m\ s^{-1} \\ \overline{\theta_l} = 288 + \Delta\theta_l - 5.5 + 0.11(z - 662.5) & K \\ \overline{q_t} = 10.2 + \Delta q_t - 1.1 - 0.022(z - 662.5) & g\ kg^{-1} \end{cases} \\
&z > 712.5\text{m} && \begin{cases} \overline{u} = -0.7 - 0.026\,(z - 662.5) & m\ s^{-1} \\ \overline{v} = -10.0 & m\ s^{-1} \\ \overline{\theta_l} = 288 + \Delta\theta_l + 6\text{x}10^{-3}(z - 712.5) & K \\ \overline{q_t} = 10.2 + \Delta q_t - 2.8\text{x}10^{-3}(z - 712.5) & g\ kg^{-1} \end{cases}
\end{aligned}
\tag{61}
$$

The initial inversion height is located around 687.5 m. The initial profile of TKE is given by:

$$0 < z < 687.5\ m \quad \overline{e} = 1\ m^2 s^{-2} \tag{62}$$

The subsidence is computed from:

$$\overline{w} = -Dz \tag{63}$$

Where D is a time dependent variable (de Roode and van der Dussen, 2010). The values of $\Delta\theta_l$ and $\Delta q_t$ in (61) were changed for different runs. The values for these runs can be found in Table 1* and Figure 13. R in Table 1 is based on equation (51). In (61) for $z > 712.5\ m$, $q_t$ would become negative if the $q_t$ jump is bigger than $-3.1\ g/kg$, which is physically impossible. So there is an extra restriction on $q_t$. If $q_t$ becomes smaller than zero, then from that point, $q_t$ is equal to zero. The resolution of the used grid is

*Exp 1 holds the same $q_t$ and $\theta_l$ jumps as the original GCSS case

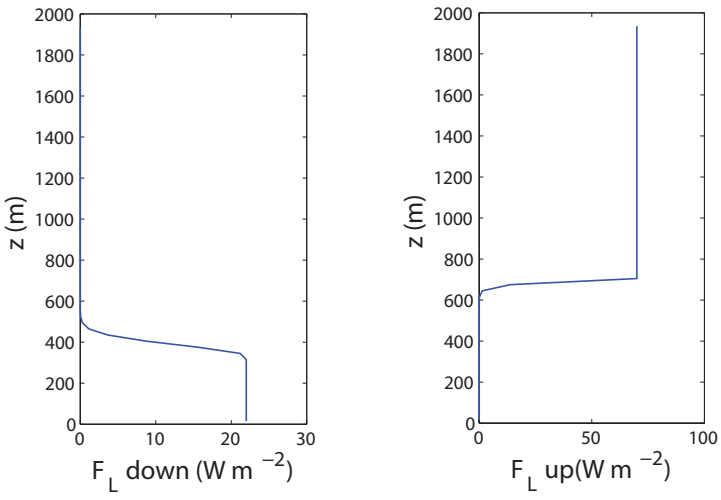


Figure 12: the initial profiles of the radiation, with on the left the longwave radiation up and on the right the longwave radiation down.

50 x 50 x 30 $m^3$ with a gridbox of 64 x 64 x 96 grid points. This gives a total domainsize of 3.2 x 3.2 x 2.8 $km^3$. The forcing that were applied can be found in table 2. The initial profiles of the longwave radiation can be found in Figure 12. DALES solves the budget equation for $\theta_l$ and $q_t$ and the navier stokes equation:

$$\rho \left( \frac{\partial \mathbf{v}}{\partial t} + \mathbf{v} \cdot \nabla \mathbf{v} \right) = -\nabla p + \nabla \cdot \sigma + \mathbf{f} \tag{64}$$

Where $\rho$ the density, **v** the flow velocity, $\sigma$ the stress tensor and **f** the body forces. The simulation follows an air package as it is advected equatorwards over increasing sea surface temperature by tradewinds. All time dependent data that comes from DALES will be hourly averaged.

Table 1: Initial values for $\Delta q_t$ and $\Delta \theta_l$

| | $\Delta q_t$ $(g/kg)$ | $\Delta \theta_l$ $(K)$ | $R$ |
|---|---|---|---|
| Exp 0 | -1.1 | 4.5 | -0.64 |
| Exp 1 | -1.1 | 5.5 | -1.01 |
| Exp 2 | -1.1 | 6.5 | -1.37 |
| Exp 3 | -2.1 | 5.5 | -0.05 |
| Exp 4 | -3.1 | 5.5 | 0.29 |
| Exp 5 | -3.1 | 7.0 | 0.09 |
| Exp 6 | -3.1 | 8.5 | -0.10 |
| Exp 7 | -3.1 | 10.0 | -0.30 |
| Exp 8 | -5.1 | 8.5 | 0.33 |
| Exp 9 | -5.1 | 10.0 | 0.21 |
| Exp 10 | -5.1 | 11.5 | 0.09 |
| Exp 11 | -5.1 | 13.0 | -0.02 |
| Exp 12 | -7.1 | 11.5 | 0.35 |
| Exp 13 | -7.1 | 13.0 | 0.26 |
| Exp 14 | -7.1 | 14.5 | 0.18 |
| Exp 15 | -7.1 | 16.0 | 0.10 |

Table 2: The forcings of DALES

| | | |
|---|---|---|
| $u_g$ | -2.0 | $m\ s^{-1}$ |
| $v_g$ | -10.0 | $m\ s^{-1}$ |
| $D$ | -0.5 | x$10^{-5}$ $s^{-1}$ |
| $z_0$ | 0.2 | $mm$ |
| $p_{surf}$ | 1029.0 | $hPa$ |
| $u_*$ | 0.3 | $m\ s^{-1}$ |

## 3.2 Determining the jumps

This thesis focuses on the effect of changes in the jumps of $q_t$ and $\theta_l$ on the evolution of a stratocumulus cloud. An example of the jumps can be seen in figure 5. The determination of these jumps has to be done carefully. The problem is that the jumps are not always well defined. The levels which are used to diagnose the jumps have to be similar for $q_t$ and $\theta_l$. The jump for $\theta_l$ was easier to determine then the jump for $q_t$. After a process of trial and error and looking at poststamp plots the jump was defined as followed:

If the gradient of $\theta_l$, for a height above $0.92$ times the inversion (provided by DALES), becomes bigger than $0.022\ g/kg\ m^-1$ it defines the inversion base height. When the gradient becomes smaller than 0.022 $g/kg\ m^-1$ it defines the inversion top.

The result of this method of determining the jump can be found inside appendix A. In this appendix poststamp plots are given for one of the runs.

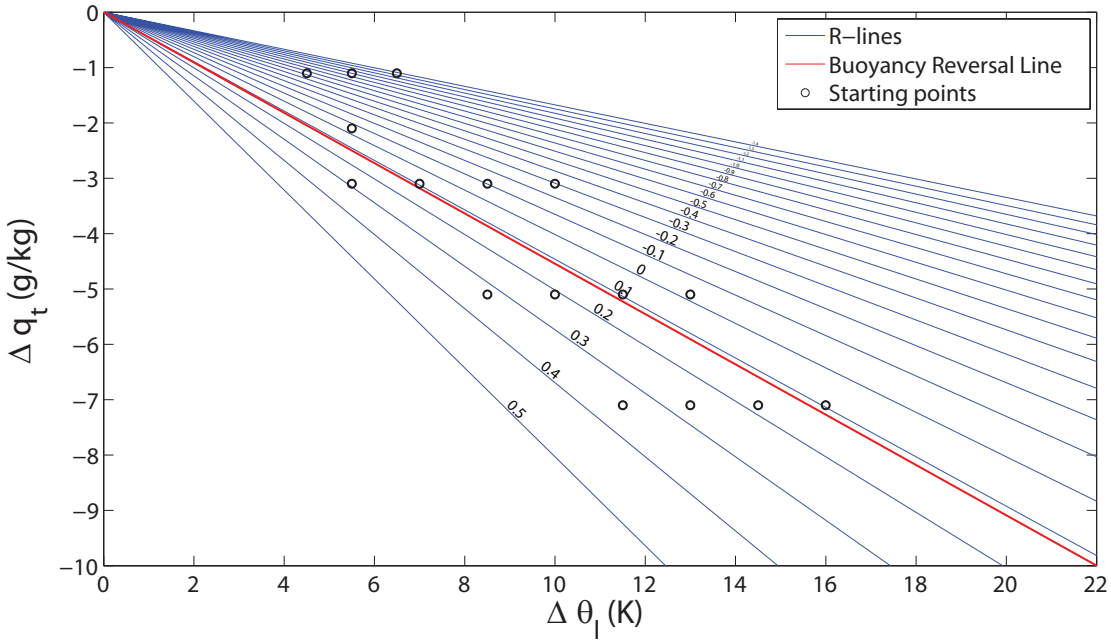


Figure 13: The initial jumps of the experiments (circles) with respect to the buoyancy reversal line (red line) and the value of R (blue lines)

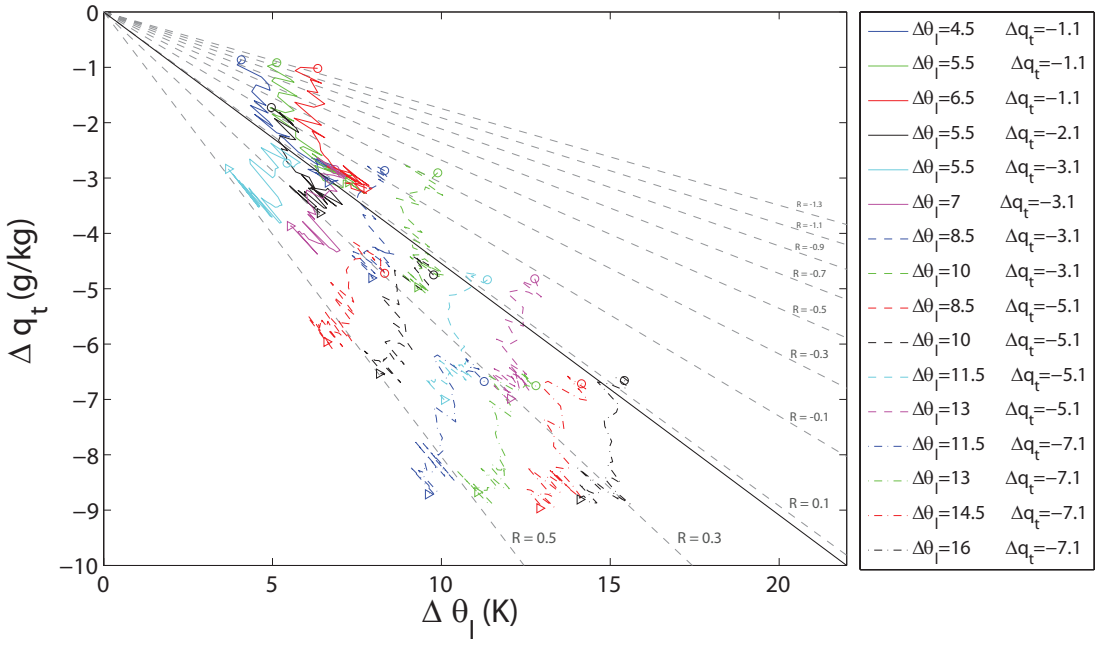


Figure 14: The course of the jumps. In the Legend the starting jumps are defined.

# 4 Results

## 4.1 The simulation

In this chapter a guide through the course of the simulation is provided. The course of the inversion jumps are indicted in figure 14. Here the open circles indicate the initial jump and the open triangles the value of the jump after 40 hours of simulation. In the legend $\Delta\theta_l$ is in $K$ and $\Delta q_t$ is in $g/kg$. This applies for all figures unless mentioned otherwise. The jumps are changing with time, because the sea surface temperature and the inversion height is increasing with time. The effect of the inversion height can be seen in Figure 15. In this figure the profiles of $\theta_l$ are plotted against the height for the three cases with $\theta_l = 0.5\ K$. In red the initial profiles of the three cases at the beginning of the simulation and in green, black and cyan the profiles after 40 hours of simulation. A total guide through the simulation is provided below. Starting with the first 6 hours between 0:00 and 6:00 then the first day between 6:00 and 18:00, the night between 18:00 and 6:00 and then the last hours 6:00 till 16:00.

### 4.1.1 The first 6 hours 0:00-6:00

Figure 16 shows the course of the inversion height with time. In the first six hours the inversion height is very dependent on the starting liquid water potential temperature jump. The lowest $\Delta\theta_l$ of each of the sets of runs with the same $\Delta q_t$ (the solid lines) have the highest inversion height. We know from equation (45) that the change in the inversion is given by the entrainment speed (see Figure 17) and the subsidence. So this can be qualitatively understood from the entrainment parameterization proposed by

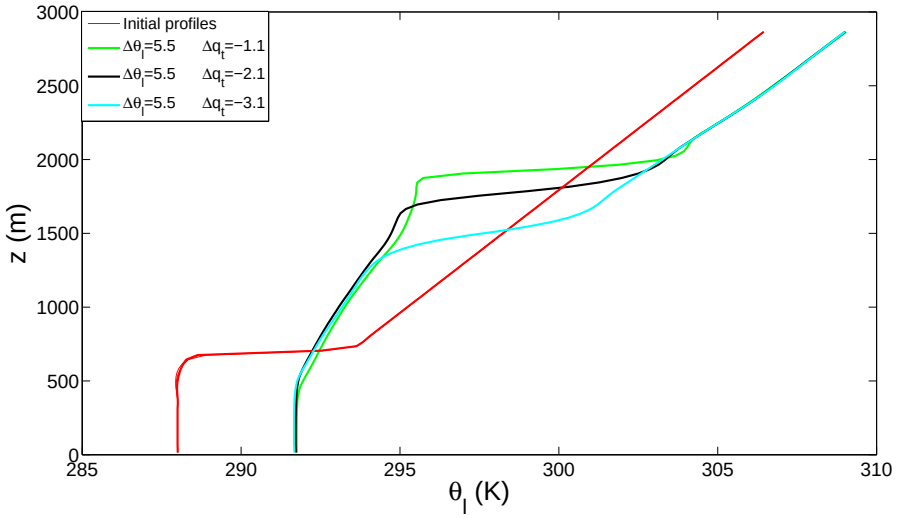


Figure 15: The profiles of $\theta_l$ with in red the initial profiles and in the other colors the profiles after 40 hours.

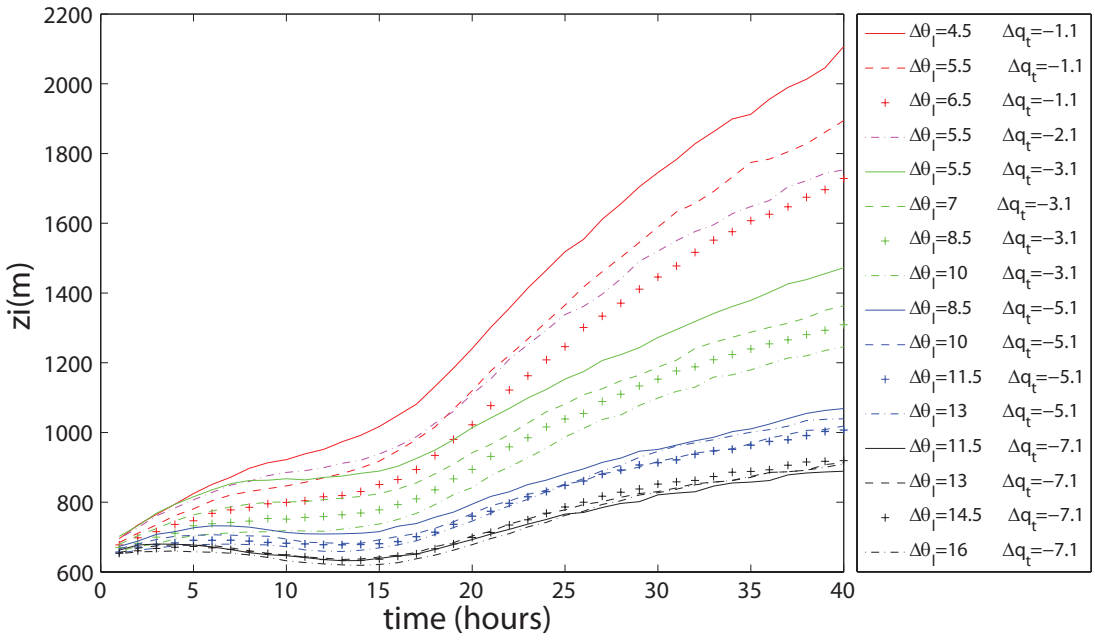


Figure 16: The inversion height over time

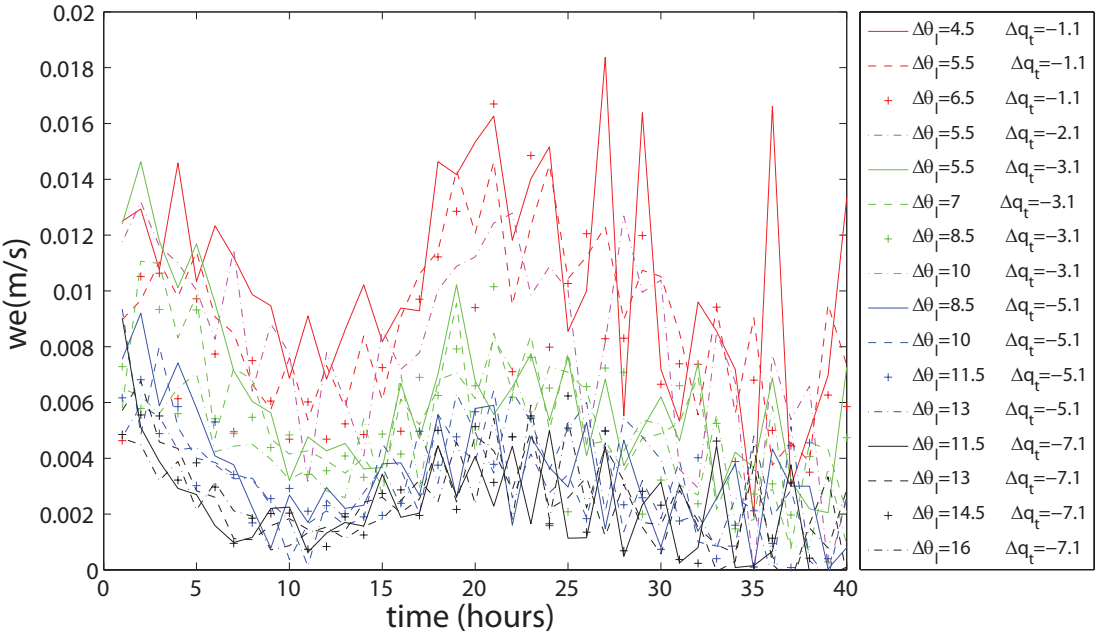


Figure 17: The entrainment velocity over time

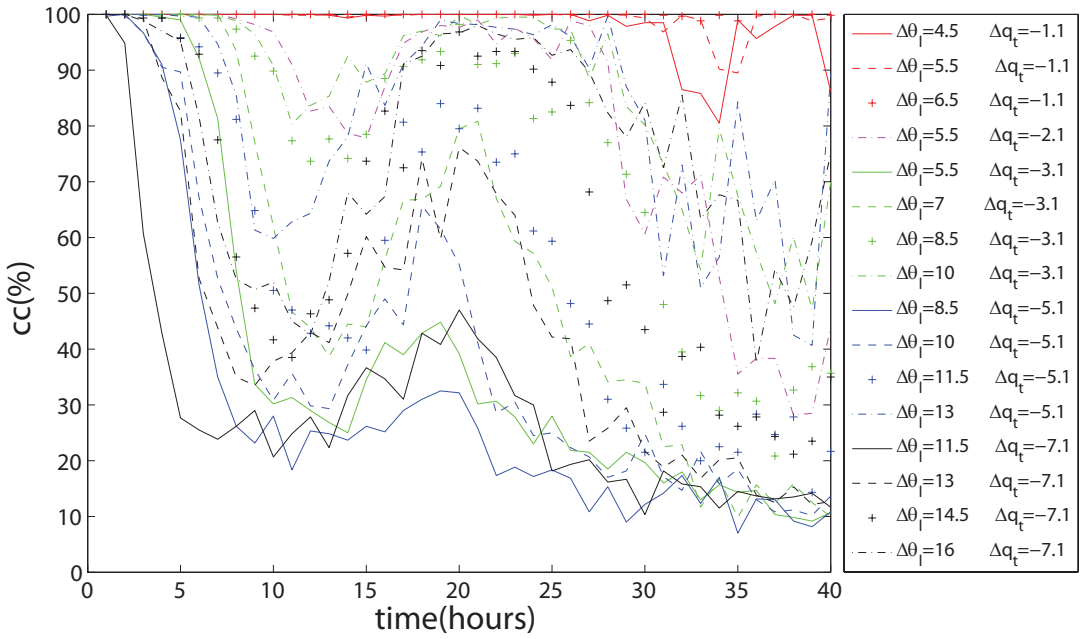


Figure 18: The cloud cover

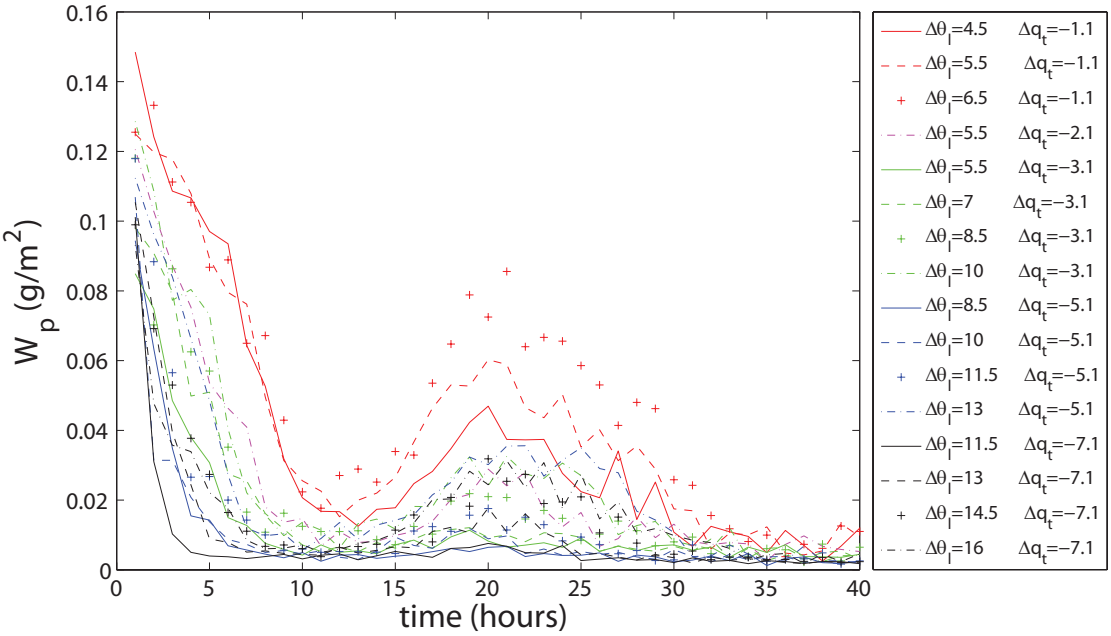


Figure 19: The Liquid Water Path

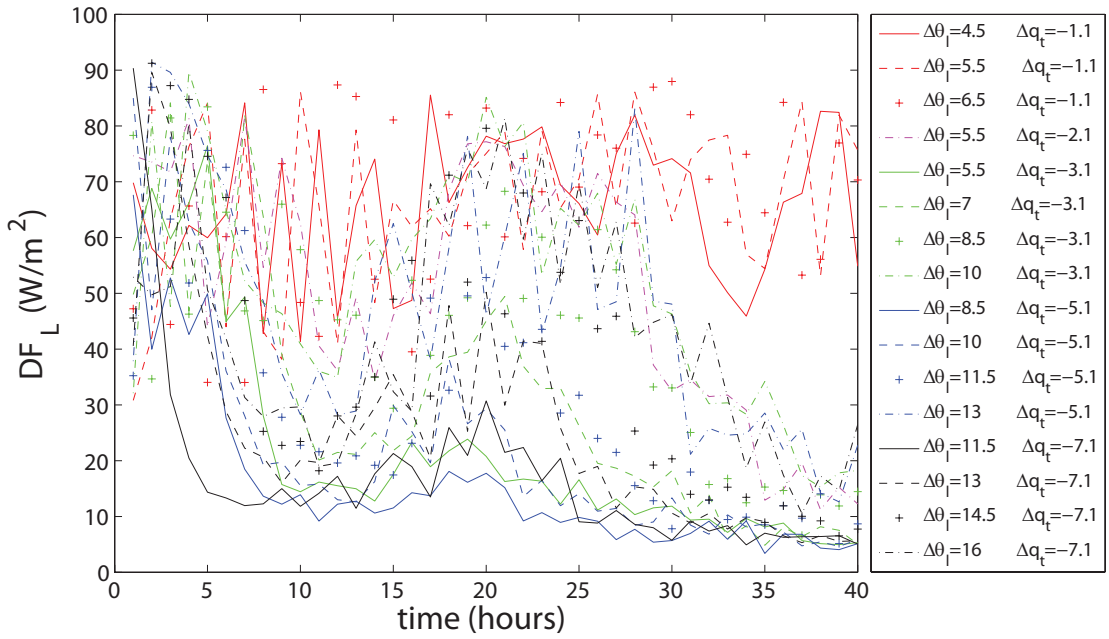


Figure 20: The change in longwave radiation between inversion and ground

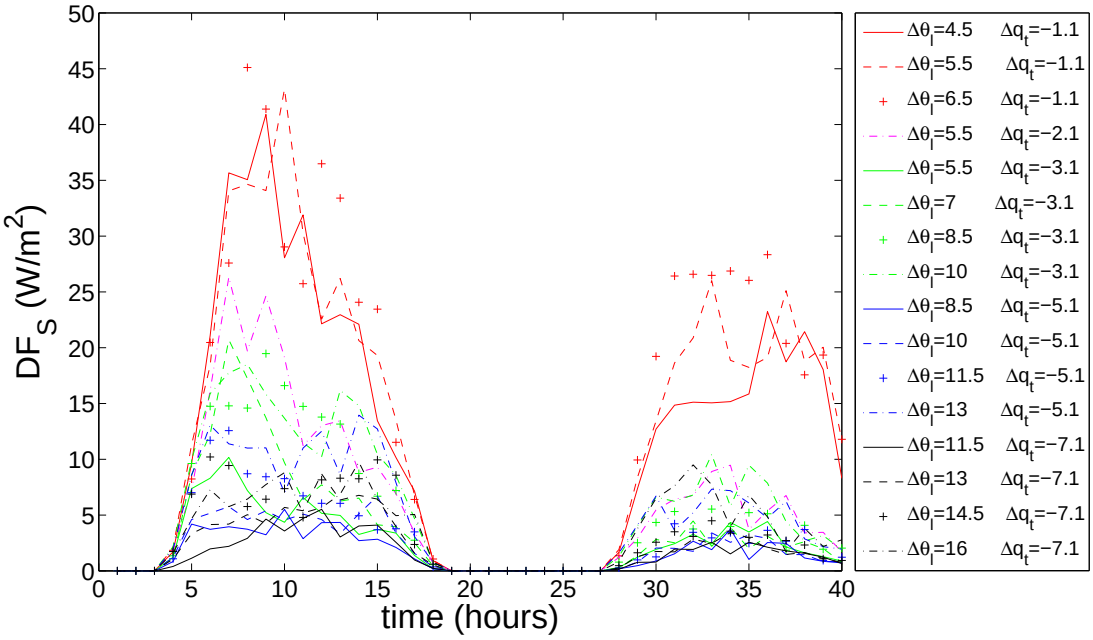


Figure 21: The absorbed shortwave radiation by the cloud

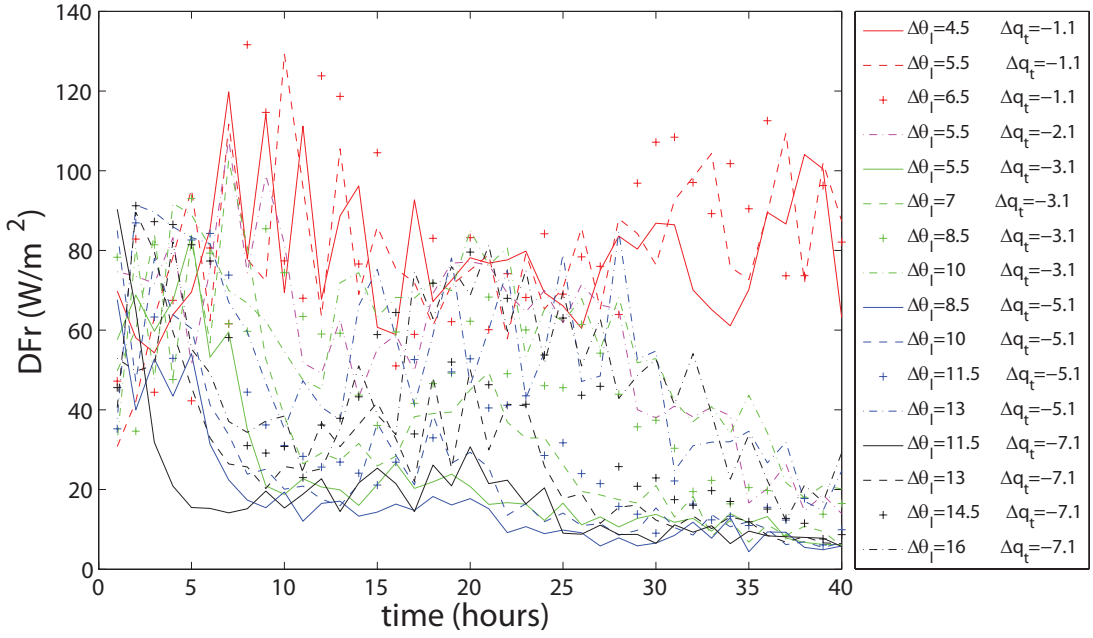


Figure 22: The change in radiation

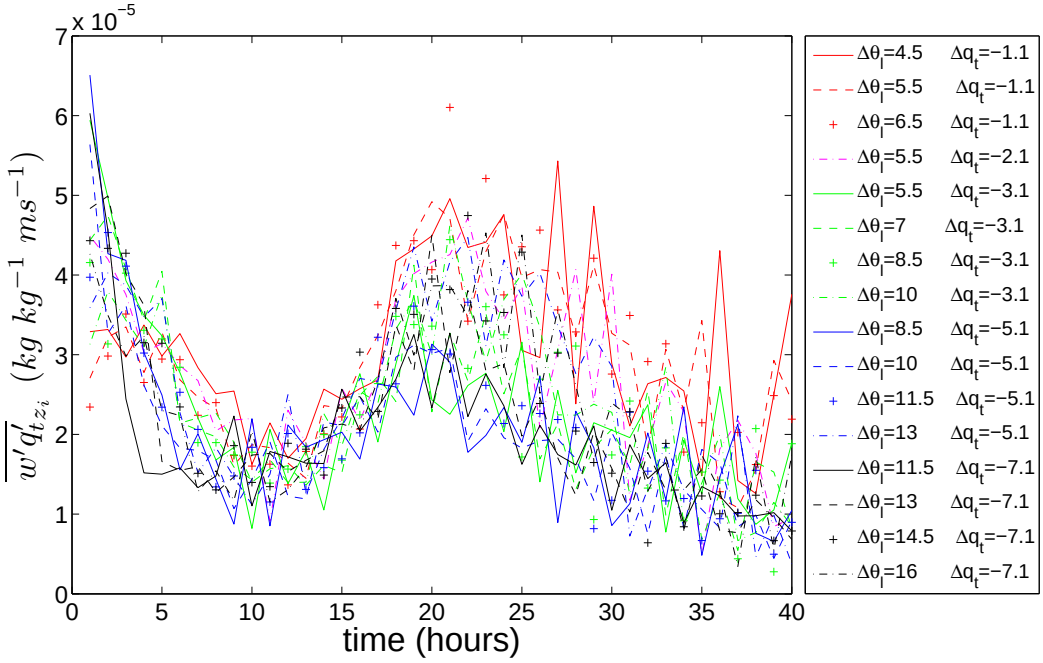


Figure 23: The $q_t$ flux at the top.

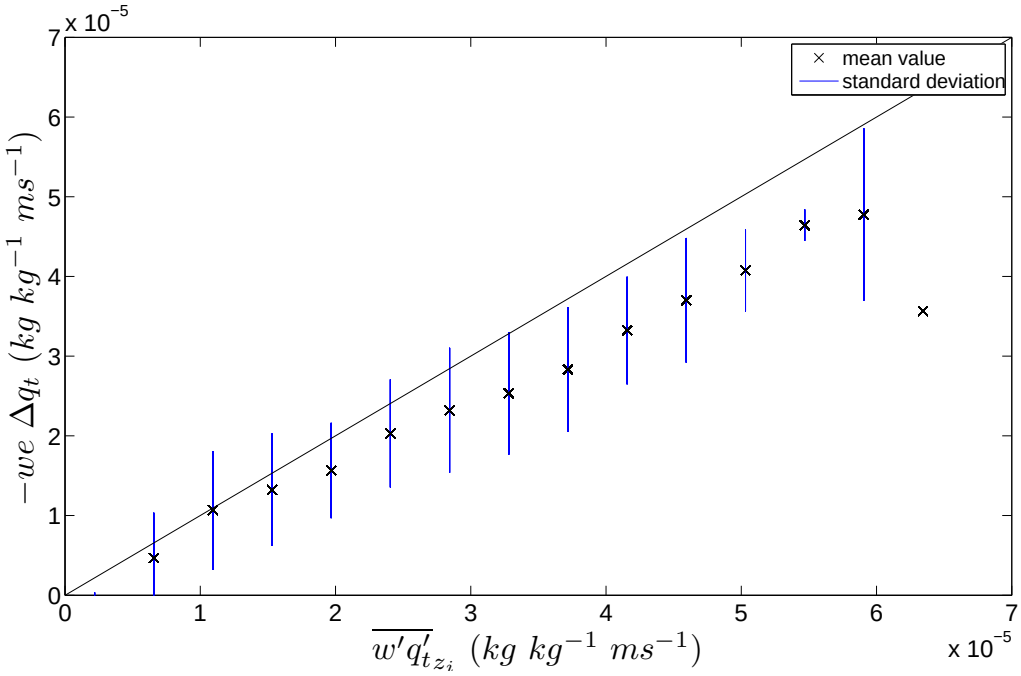


Figure 24: The $q_t$ flux at the top against the $q_t$ flux calculated by equation (38)

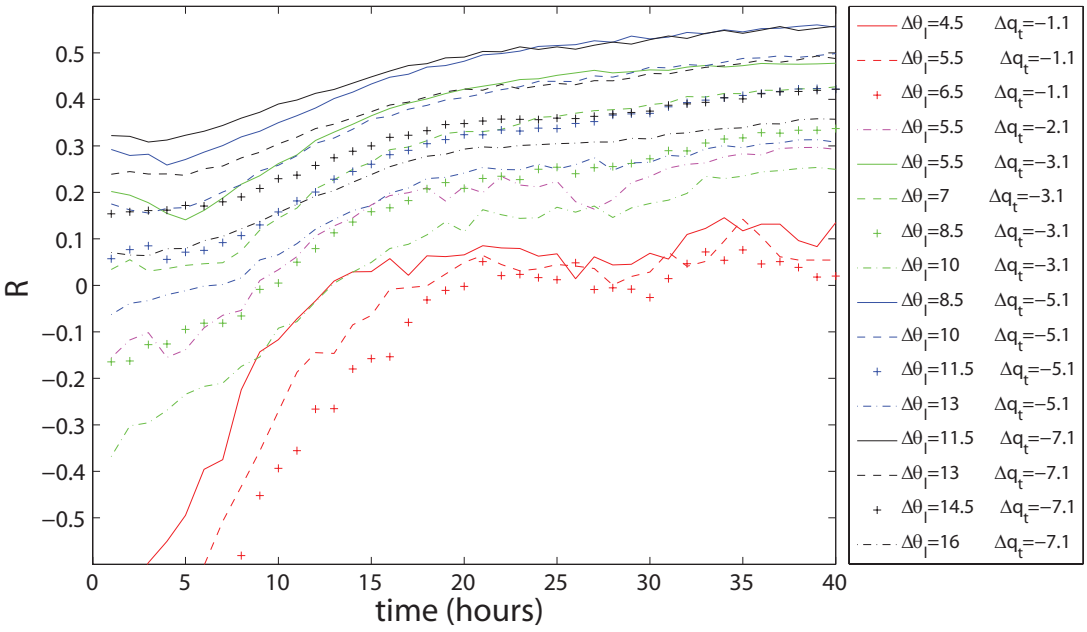


Figure 25: The parameter that indicates buoyancy reversal (R) vs time

Moeng (equation (43)). The entrainment becomes smaller for larger values of $\Delta\theta_l$. This would explain why they are divided by the $\theta_l$ jump. For simulations that started far below the buoyancy reversal line, the cloud cover has dramatically decreased in this first 6 hours (see figure 18). The cloud of the $\Delta q_t = -7.1$ $g/kg$, $\Delta\theta_l = 11.5$ $K$ simulation only has a cloud cover of 30% left after 5 hours. Followed by the $\Delta q_t = -5.1 g/kg$, $\Delta\theta_l = 8.5$ $K$ simulation, that goes below 30% after 7 hours. This conforms the idea that below this line, stratocumulus clouds do not exist. They only started as stratocumulus, because they are initialized as stratocumulus.

### 4.1.2 The first day 6:00-18:00

The effect of the sun and it's shortwave radiation (Figure 21) is visible from Figure 22 for the cases with starting $|\Delta q_t| > 1.1$. Here the shortwave radiation starts to compensate the longwave radiation, which means that the net radiation goes down. This should mean that the entrainment rate would go down (which is true, see Figure 17) and that means the inversion rises less (which is also true, see Figure 16). The inversion height is now more dependent on the humidity jump. This is however obviously not included in Moeng's parameterisation. However this can be understood by looking at equation (38). The $\Delta\theta_l = 4.5$ $K$, $\Delta q_t = -1.1$ $g/kg$ case has the highest $q_t$ flux (see Figure 23) and smallest $\Delta q_t$ (and smallest $\Delta\theta_l$) and so the highest entrainment (Figure 17). Therefore it has the highest inversion. Followed by the $\Delta\theta_l = 5.5$ $K$, $\Delta q_t = -1.1$ $g/kg$ case, then the $\Delta\theta_l = 6.5$ $K$, $\Delta q_t = -1.1$ $g/kg$ and so on. To check if equation (38) can be used it has been plotted against the $q_t$ flux at the top provided by DALES. This can be seen in Figure 24. It follows that till $\overline{w'q'_{t_{z_i}}} = 3$ $kg$ $kg^{-1}$ $ms^{-1}$ it holds. For higher values of $\overline{w'q'_{t_{z_i}}}$ there is a slight ofset. During the day it is possible for turbulence in the cloud layer to become decoupled from turbulence in the bottom of the subcloud layer (Turton and Nicholls,

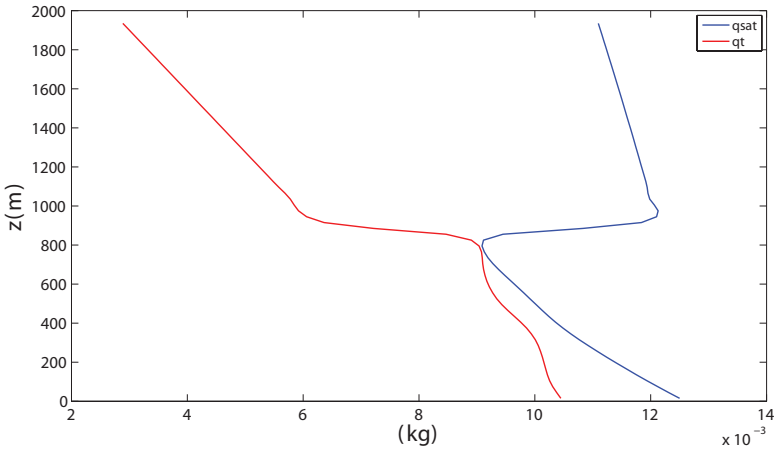


Figure 26: The $q_t$ $(kg)$ and $q_{sat}$ $(kg)$ profiles at the 8th hour of simulation $\Delta q_t = -3.1g/kg$, $\Delta\theta_l = 5.5K$

1987). In Figure 25 we can see that during the day some simulations go below the buoyancy reversal line, which means that there is this extra turbulence. More dry and warm air is entrained from above the inversion, which leads to break up from the cloud. Figure 18 supports this. All the cases that go below the buoyancy reversal line lose their 100 percent cloud cover. In DALES a cloud tends to break up if the buoyancy reversal criteria is satisfied. This is not always found in observations (B. Stevens, 2003). Around 15:00 the effect of the sun's shortwave radiation is already weakened (see Figure 21). From this time the entrainment starts to increase and the clouds are starting to rise. Also the cloud cover increases again. The cases furthest below the buoyancy reversal line are now almost shallow cumulus clouds. Between 8:00 and 9:00 the cloud of the $\Delta q_t = -3.1g/kg$, $\Delta\theta_l = 5.5K$ case has disappeared. This can be made more clear by looking at figure 26 here we can see that $q_t$ and $q_{sat}$ don't have a overlap with each other at the 9th hour.

### 4.1.3 The night 18:00-6:00

Now the longwave radiation dominates again in $DF_R$ (see Figures 20 and 21). This means that the entrainment speed increases and the cloud top goes up (see Figure 16 and 17). The inversion height of the different cases is not as ordered by $\Delta\theta_l$ as it was 18 hours ago. The simulation with a smaller $q_t$ jump the ordering is still the same (the red, purple and the green lines in Figure 16). The cases with the largest $q_t$ jumps cluster together at the same height. For those cases the cloud holds little water (see Figure 19), which means the cloud radiates less longwave radiation, which means less entrainment and so finally this means they do not go much higher. This effect probably also causes the dashed cases (except for the red one) and the case indicated by the blue plus to lose their cloud cover after eight (see Figure 18 and 20). Because the simulations with the smallest $q_t$ jump (red and lines in Figure 16) still have a 100 percent cloud cover they still emit a lot of longwave radiation and so still rise fast. Around four (28 hours of simulation) the sun starts to shine again and shortwave radiation starts to play it role again. At this time only the cases with the smallest $q_t$ jump did not pass the buoyancy reversal line.

#### 4.1.4 The last few hours 6:00-16:00

The shortwave radiation compensates the longwave radiation and turbulence is created inside the cloud. Finally after 33 hours of simulation the $\Delta q_t = -1.1g/kg$, $\Delta\theta_l = 4.5K$ and $\Delta q_t = -1.1g/kg$, $\Delta\theta_l = 5.5K$ cases go below the buoyancy reversal line and lose their 100 percent cloud cover. The inversion heights of the simulations with the initial smallest two $q_t$ jumps are still ordered by $\Delta\theta_l$ like in the beginning.

### 4.2 Buoyancy reversal

#### 4.2.1 Cloud cover and buoyancy reversal

As can be seen from the previous result, buoyancy reversal is an important process for determine the break up of the cloud. In Figure 27 the cloud cover above the buoyancy reversal line is visible higher than below. These results have been binned and averaged and plotted with the standard deviation in Figure 28. This is a figure comparable to that of Lock's (Figure 7). It becomes clear from this figure that the cloud cover starts to drop (almost linear with R) when $R$ becomes smaller than $0.1$. This is not a big surprise. The buoyancy reversal criteria is met at R equal to 0.1 (see Figure 13). Figure 28 also supports Lock's conclusion. For $R \leq 0.2$ cloud covers of 80% or more seem to occur. If $R \geq 0.5$ only shallow cumulus appear (with a cloud cover of 20% or less). However the spread in the result from this thesis is bigger than the spread from the result of Lock's paper. Lock's results all fall nicely into almost one curve, but even if the results from this thesis are averaged per case, still a spread can be seen (Figure 29).

#### 4.2.2 Entrainment and buoyancy reversal

In Figure 30 the entrainment is plotted against value R. In the left figure we can clearly see that at night the entrainment velocity is higher. This is due to the fact that at night is more radiative cooling. The right figure shows that the entrainment speed goes up as $R$ comes closer to $0.1$. At $R = 0.1$ the standard deviation is $0.0045\ (m/s)$, which is relatively big. This might be because for some cases the cloud might already be decoupled, while for some cases the cloud is not decoupled yet. As $R$ now becomes bigger, for more cases the clouds are decoupled and so the entrainment goes down.

#### 4.2.3 Liquid water path and buoyancy reversal

The results here should be coherent with the results of the cloud cover. And according to Figure 31, they are. Around $R = 0.1$ the LWP rapidly decreases. This is most clear from the night time results. Interesting to see is that that drop already occurred at $R = 0$, for the daytime results.

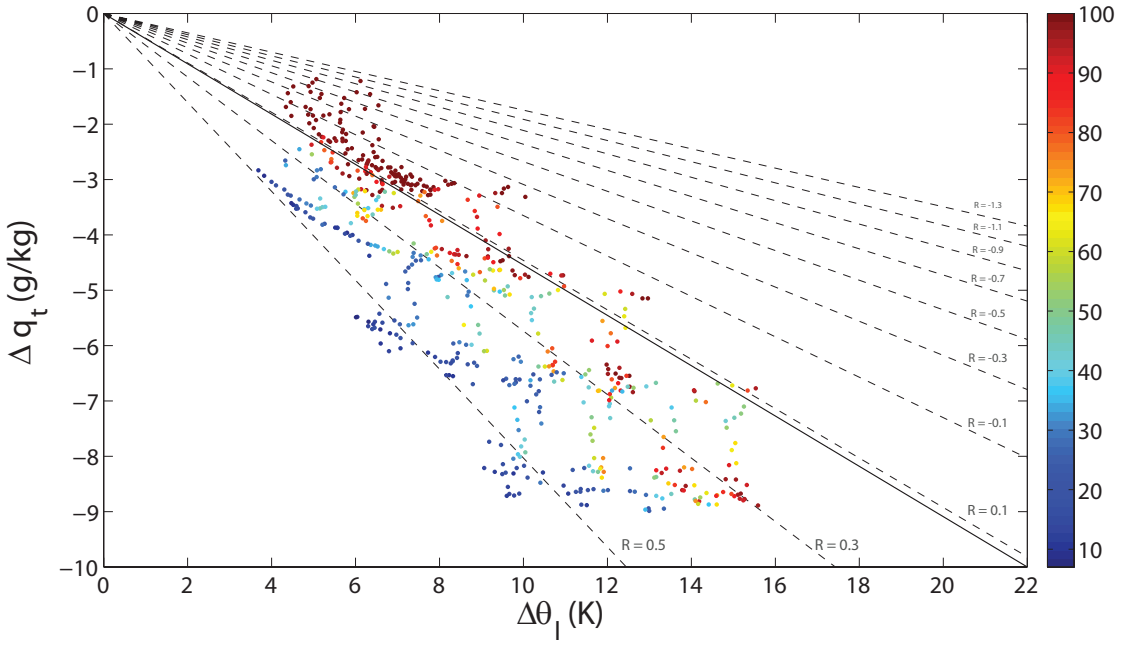


Figure 27: A scatter plot of the cloud cover (cc) vs $\Delta q_t$ and $\Delta\theta_l$

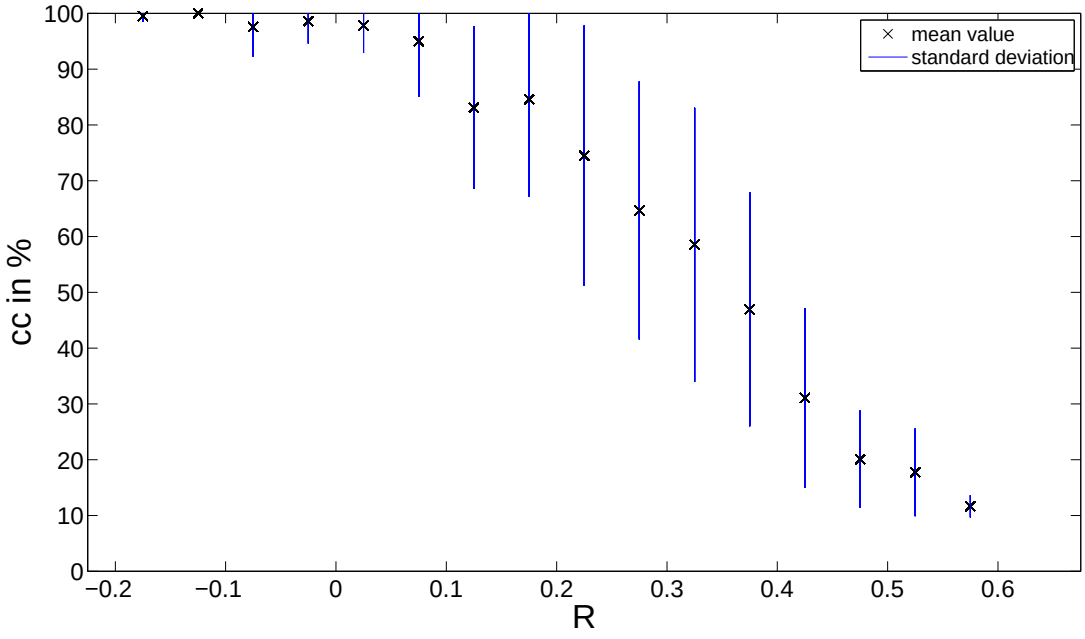


Figure 28: The cloud cover vs parameter R, binned and averaged, the first three hours excluded

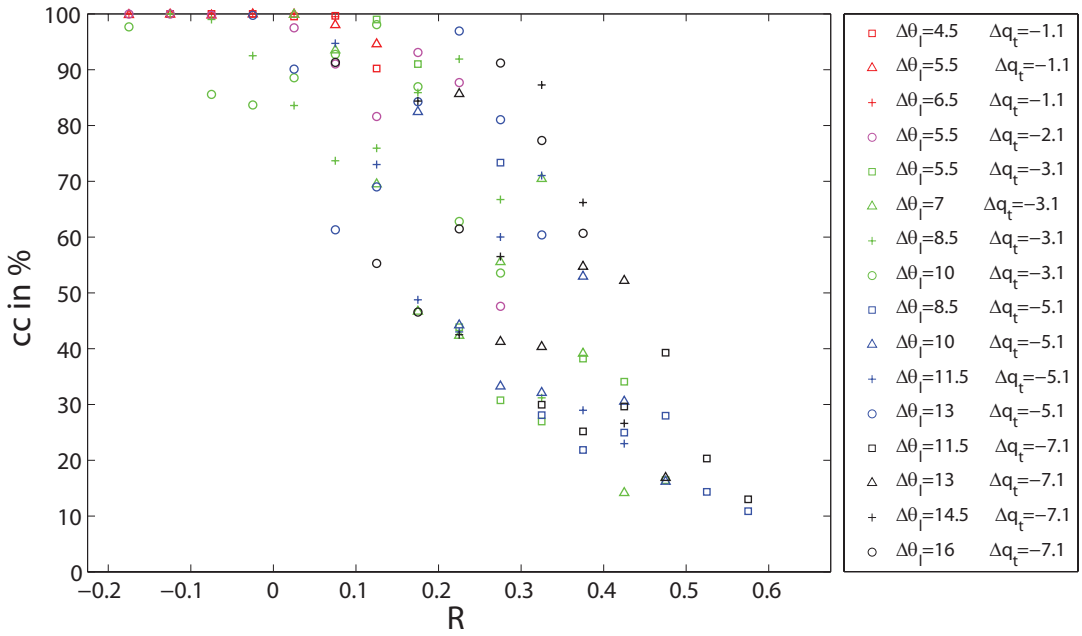


Figure 29: The cloud cover vs parameter R, binned and averaged per case, the first three hours excluded

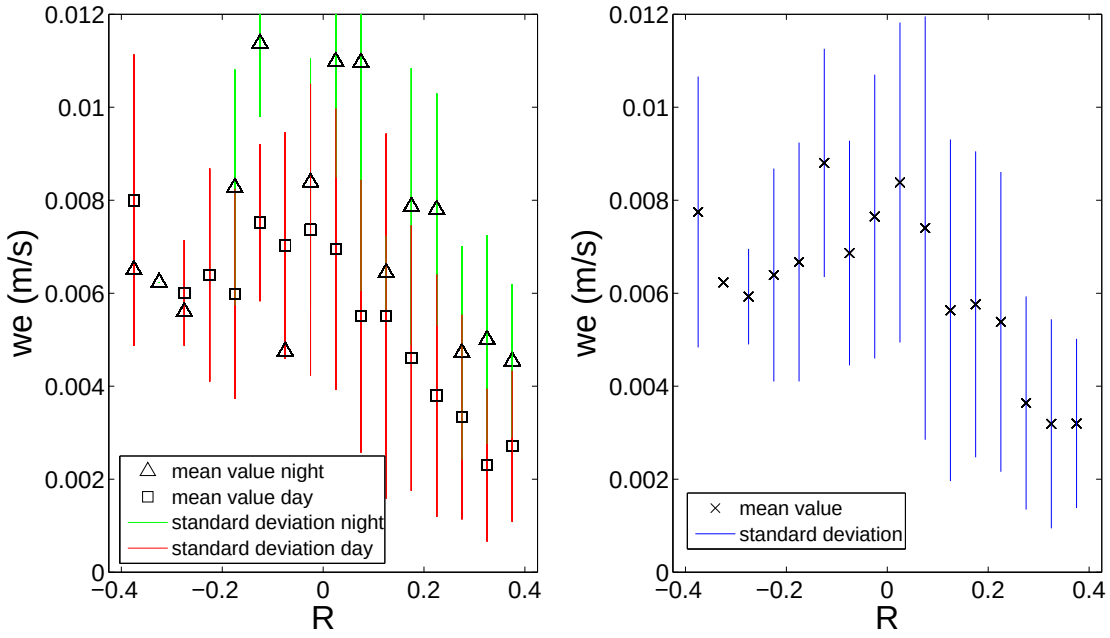


Figure 30: The entrainment rate versus parameter R, binned and averaged. With on the left a distinction is made between night (first 3 hours and hour 18 till 27) and day (4th hour till 17th hour and 28th hour till 40th hour). On the right side the mean of the total simulation

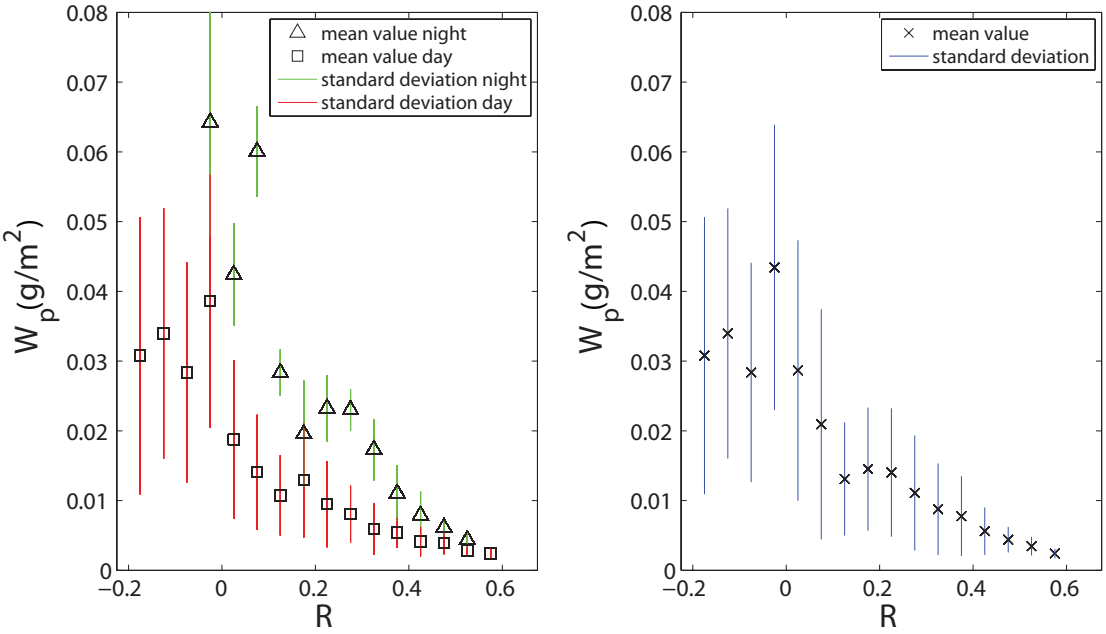


Figure 31: Parameter R vs the LWP. binned and averaged, the first three hours excluded

### 4.2.4 The virtual potential temperature flux

The virtual potential temperature flux ($\overline{w'\theta_v'}$) is driving turbulence and entrainment, thats why it would be interesting to take a better look. Below three cases will be shown. The first one is a case for which the cloud did not break up and was furthest above the buoyancy reversal line. The $\Delta\theta_l = 6.5\ K$, $\Delta q_t = -1.1\ g/kg$ case. In Figure (32) $\overline{w'\theta_v'}$ is plotted against the time and height. The second case is one that started above the buoyancy reversal line and ended op below it after around 15 hours. The $\Delta\theta_l = 8.5\ K$, $\Delta q_t = -3.1\ g/kg$ case. This one is plotted in Figure 33. The third case started furthest below the buoyancy reversal line. The $\Delta\theta_l = 11.5\ K$, $\Delta q_t = -7.1\ g/kg$ case, plotted in Figure 34. During the day the flux at the top is almost zero. Which is not surprising, because at that time the absorbs the most shortwave radiation (see Figure 21). At night the turbulent flux of $\theta_v$ becomes much higher (more negative). This will generate turbulence witch moistens the cloud. The second case (which crosses the buoyancy reversal after approximately 15 hours) clearly has a flux near zero during the day. It has a minimum around noon (for the first day). At night the cloud moistens and higher values for $\overline{w'\theta_v'}$ can be detected. The cloud almost goes back to a 100% cloud cover (see Figure 18). In the cloud layer the highest buoyancy fluxes can be found. This is caused by the warming effect of the condensation of water vapor, that rises from the surface. And because at night there is radiative cooling, higher fluxes can be found inside the cloud layer at night. During the day the buoyancy flux in the cloud layer is much lower. There also needs to be a cloud in order to have radiative cooling and so a higher buoyancy flux in the cloud layer. This is what happens in the third case. The third case begins as a stratocumulus cloud, but after 4 hours the cloud is already almost vanished. A cloud cover of 30% remains (Figure 18). Almost no turbulant flux of $\theta_v$ can be seen from Figure 34. The same happens after 28 hours in case 2. In case two and three we should have seen a positive flux at the cloud's top, as they both pass the buoyancy reversal line. A reason why this might not be seen is these values are horizontal avarages.

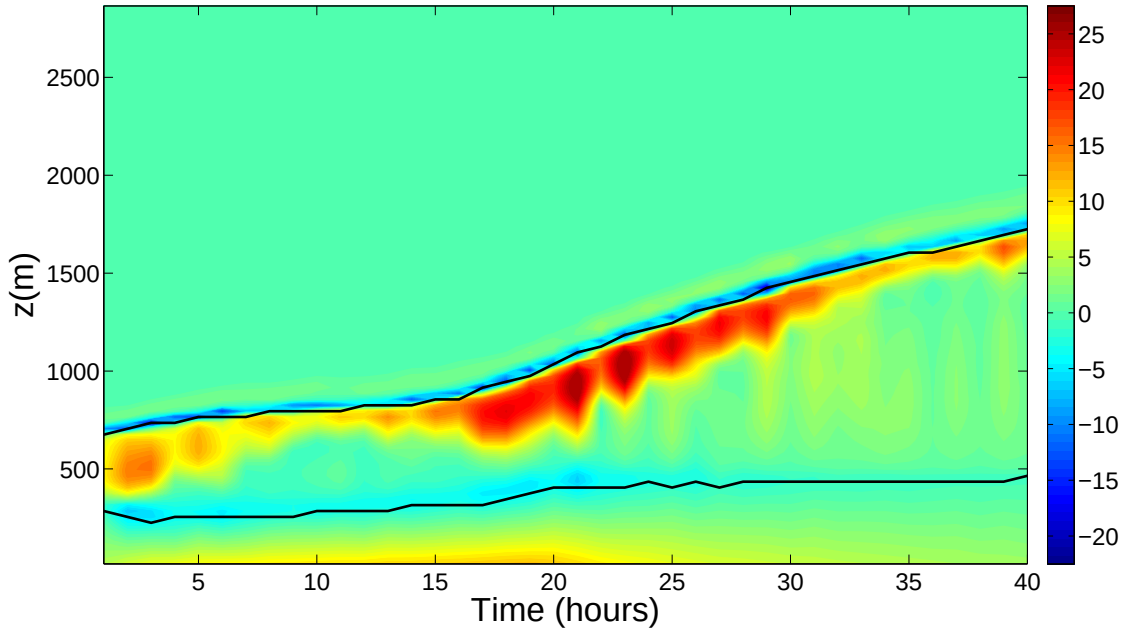


Figure 32: A contourplot of the turbulent flux of $\theta_v$ in $Wm^{-2}$ as a function of height and time for the $\Delta\theta_l = 6.5\ K$, $\Delta q_t = -1.1\ g/kg$ case. The black lines indicate the cloud top and minimum cloud base

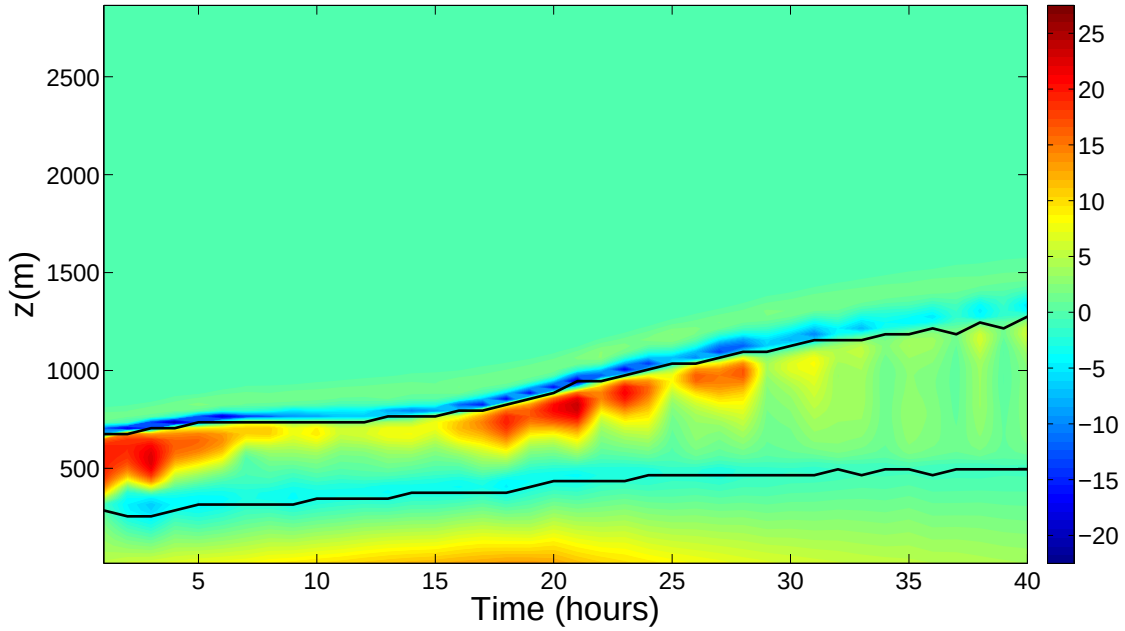


Figure 33: A contourplot of the turbulent flux of $\theta_v$ in $Wm^{-2}$ as a function of height and time for the $\Delta\theta_l = 8.5\ K$, $\Delta q_t = -3.1\ g/kg$ case. The black lines indicate the cloud top and minimum cloud base

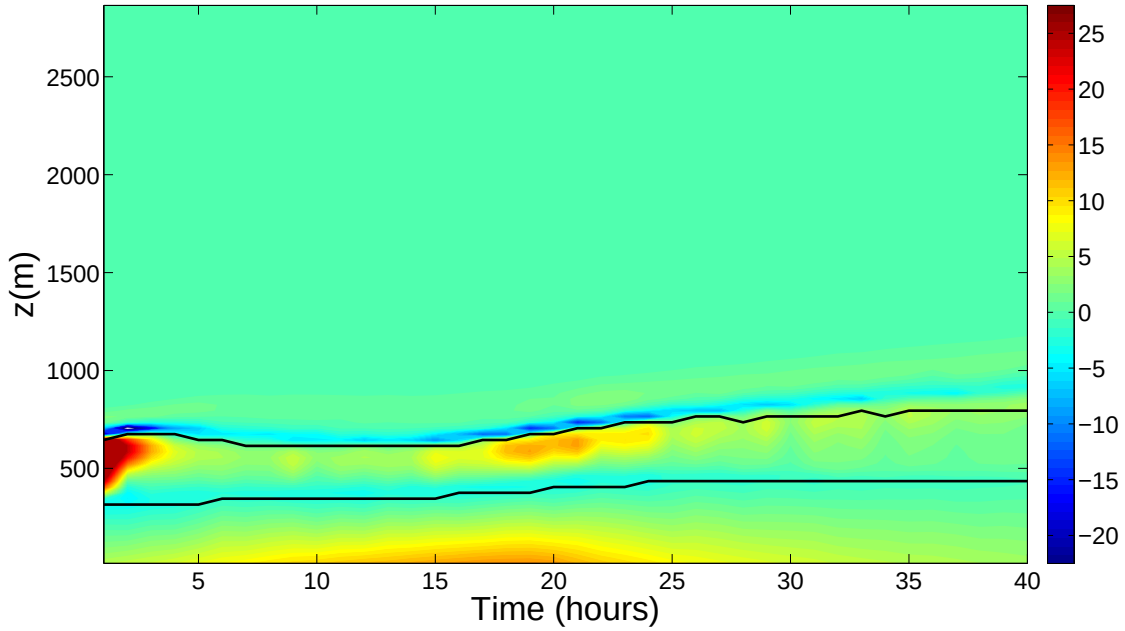


Figure 34: A contourplot of the turbulent flux of $\theta_v$ in $Wm^{-2}$ as a function of height and time for the $\Delta\theta_l = 11.5\ K$, $\Delta q_t = -7.1\ g/kg$ case. The black lines indicate the cloud top and minimum cloud base

### 4.2.5 Cases with the same initial R

In this thesis some simulations were done with (almost) the same value of R. It would be interesting to look how far they ended from each other. If they end up close something could be said about the development of a cloud if the initial value R is know. The following cases will be discussed:

Table 3: Cases with almost the same initial values, with $\Delta\theta_l$ in $K$ and $\Delta q_t$ in $g/kg$

| | | | | |
|---|---|---|---|---|
| Case 1 | $\Delta\theta_l = 5.5, \Delta q_t = -2.1$ | $R \approx -0.05$ | $\Delta\theta_l = 13.0, \Delta q_t = -5.1$ | $R \approx -0.02$ |
| Case 2 | $\Delta\theta_l = 5.5, \Delta q_t = -3.1$ | $R \approx 0.29$ | $\Delta\theta_l = 13.0, \Delta q_t = -7.1$ | $R \approx 0.26$ |
| Case 3 | $\Delta\theta_l = 7.0, \Delta q_t = -3.1$ | $R \approx 0.09$ | $\Delta\theta_l = 11.5, \Delta q_t = -5.1$ | $R \approx 0.09$ |
| | $\Delta\theta_l = 16.0, \Delta q_t = -7.1$ | $R \approx 0.1$ | | |
| Case 4 | $\Delta\theta_l = 8.5, \Delta q_t = -5.1$ | $R \approx 0.33$ | $\Delta\theta_l = 11.5, \Delta q_t = -7.1$ | $R \approx 0.35$ |
| Case 5 | $\Delta\theta_l = 10, \Delta q_t = -5.1$ | $R \approx 0.21$ | $\Delta\theta_l = 14.5, \Delta q_t = -7.1$ | $R \approx 0.18$ |

It is clear that nothing can be said over the inversion height, by only looking at parameter R. The inversion height is, as concluded before very dependent on $\Delta q_t$. Much more than on $\Delta\theta_l$. So let's focus on the cloud cover and R over time. These are plotted again in Figure 35 and 36, but now matched per case, to get a clearer view. At first sight case one is not a match. During the day both diverge from each other. But what is interesting is that their cloud covers start to fall at the same time. However, this is after 27 hours, exactly the time the sun starts to shine again. The cloud cover of the simulation with starting values $\Delta\theta_l = 5.5\ K$, $\Delta q_t = -2.1\ g/kg$ also decreases further. The second case is also not a match. The cloud cover hugely differs (at hour 20 it differs 37%). They cluster together at the end, but that is only

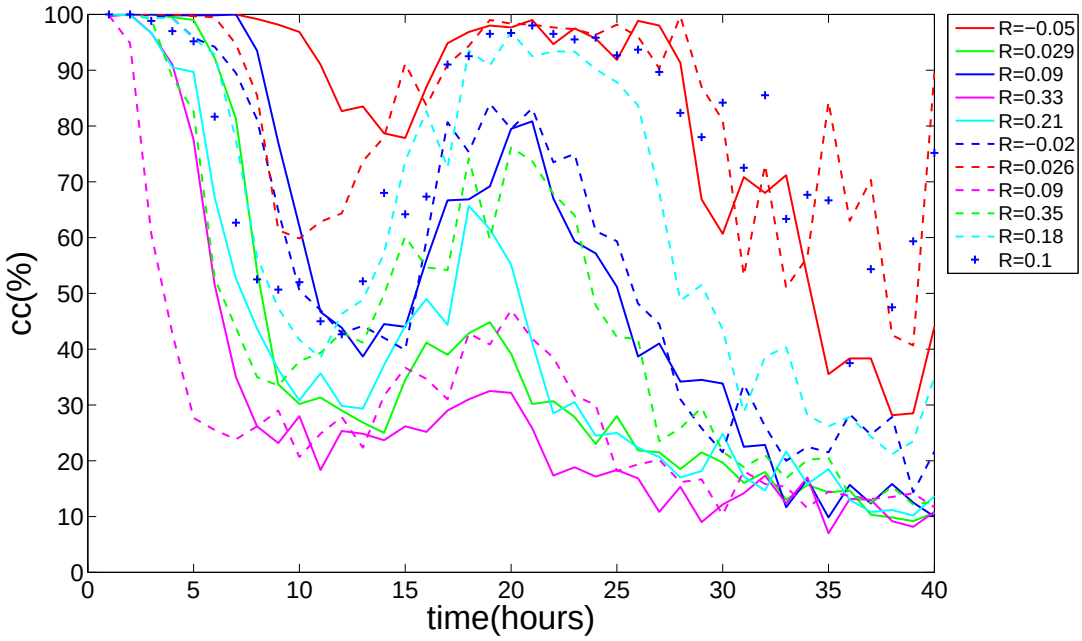


Figure 35: The cloud cover as a function of time, with cases matched together

because they are both almost dissolved. Finally at case 3 we find an agreement between two simulations. The simulation with starting $R = 0.1$ does not match, but the only two simulations we had with the same intial R follow each other closely. The biggest difference they make is 15%. The two simulations in Case 4 also stay close to each other, but both clouds are dissolved quite fast. At the end all cases with high R values will be close to each other. The same for small values of R as for them the cloud cover is always a 100%. The last case is also not hopefull. A difference of almost 65% can be spotted after 22 hours of simulation. In Figure 36 the R value of the cases have been plotted against time. This gives the same image as the cloud cover did. Both simulations with $R = 0.09$ do not differ much from each other. After 15 hours of simulation the simulations of Case 2 have almost the same R. The reason, however, can be that both clouds have been (are almost) dissolved around that time.

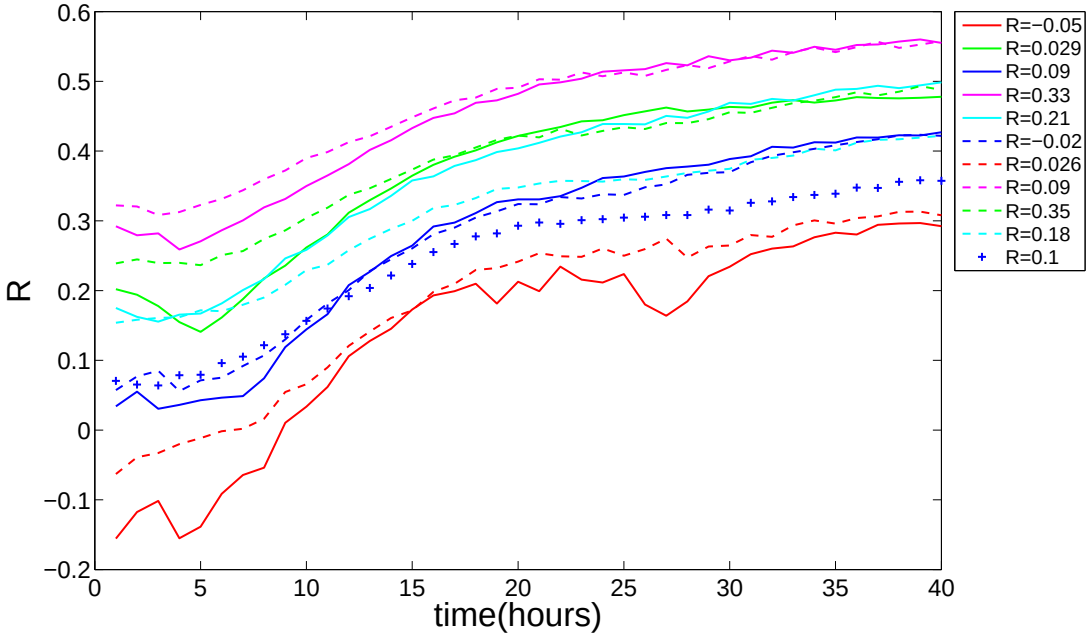


Figure 36: The cloud cover as a function of time, with cases matched together

# 5 Conclusion and recommendation

This chapter will be split up into two parts. The first part will show the conclusions made on basis of the results of previous chapter. The second part will be a recommendation on how this research can evolve further.

## 5.1 Conclusions

### 5.1.1 Inversion and entrainment

*(i) The values of the starting humidity jump ($\Delta q_t$) and the liquid water potential jump ($\Delta \theta_l$) have a great impact on the height of the inversion.* The height of the inversion is dominated by the size of $\Delta q_t$. The smaller the humidity jump is, the higher is the entrainment and so the higher the inversion will be. This can be explained by a larger total water flux at the cloud top by turbulent mixing. The same accounts for $\Delta \theta_l$, however these changes are smaller and are explained by the parameterisation of Moeng.

### 5.1.2 Buoyancy Reversal

*(i) According to DALES, the buoyancy reversal line is a good indicator to check if stratocumulus clouds can exist.*Below the buoyancy reversal the clouds start to break up. However caution is advised as DALES tends to let clouds break up as they passed this line. This is not always found in observations (B. Stevens, 2003)

*(ii) Data from DALES supports the findings of A.P. Lock in his paper "Factors influencing cloud area at the capping inversion for shallow cumulus clouds" in 2008.* Lock found that for $R \leq 0.2$ cloud covers of 80% or more seem to occur, while for $R \geq 0.5$ only shallow cumulus appear (with a cloud cover of 20% or less). DALES supports this, however the spread in the data from DALES is larger than that of A.P. Lock.

*(iii) The entrainment rate increases when getting closer to the buoyancy reversal criteria.* An increasment of $0.02\ m/s$ can be detected when going from R=0.4 to R=-0.1. After that it drops significantly.

*(iv) Cases with almost the same initial value of R do not have a similar trajectory of cloud cover or R over time.* In five comparisations, where within each comparisation the initial R of two simulations didn't differ more than 0.03, only one comparisation was similar. This was a comparisation of two cases with both approximately an R value of 0.09.

*(v) From contour plots of the turbulent flux $\theta_v$ the buoyancy reversal criterion can not be seen.* This might be, because the values presented there are horizontal averaged.

## 5.2 Recommendations

There are three important recommendations for further research to be made.
**One**: More grid points should be used to get a better detailed look at the results and to see if it then still supports our results.
**Two**: A better way of determining the humidity and liquid water potential temperature jump has to be found. This research is very dependent on this two values and small difference in $\Delta q_t$ and $\Delta \theta_l$ can lead to big change somewhere else.
**Three**: Other models could be used for the same simulations, because DALES tends to break up clouds after they pass the buoyancy reversal criteria, this is not always found in observations (B. Stevens, 2003).
At last it could also be interesting to research more case with exact the same value of R. The two simulation with the same value of R that was represented in this report showed similarities to each other by looking at the cloud cover and their distance to the buoyancy reversal line.

# References

[1] D. Johnson W.H. Schubert B.A. Albrecht, C.S. Bretherton and A.S. Frisch. The atlantic stratocumulus transition experiment − ASTEX. *Bulletin of the American Meteorological Society*, 76:889−904.

[2] A. Chlond and A. Wolkau. Large-Eddy Simulation Of A Nocturnal Stratocumulus-Topped Marine Atmospheric Boundary Layer: An Uncertainty Analysis, 1999.

[3] S. Nicholls D.A. Bennetts, E. McCallum and J.R. Grant. Stratocumulus: an introductory account. *The Meteorological Magazine*, 115(1-2):65−76, 1986.

[4] S.R. de Roode. Clouds, 2004.

[5] S.R. de Roode and P.G. Duynkerke. Observed lagrangian transition of stratocumulus into cumulus during ASTEX: mean state and turbulent structure. *Journal of the Atmospheric Sciences*, 54:2157−2173, 1997.

[6] S Bony, J.L. Dufresne. An Assessment of the Primary Sources of Spread of Global Warming Estimates from Coupled Atmosphere Ocean Models. *Journal of Climate*, 21:5135−5144, 2008.

[7] A.P. Lock. Factors influencing cloud area at the capping inversion for shallow cumulus clouds. *Q.J.R. Meteorol. Soc.*, 00:1−12, 2008.

[8] R. B. Stull. *An Introduction to Boundary Layer Meteorology*. Kluwer Academic Publishers, 1988.

[9] B. Stevens, D. H. Lenschow, G. Vali, H. Gerber, A. Bandy, B. Blomquist, J.-L. Brenguier, C. S. Bretherton, F. Burnet, T. Campos, S. Chai, I. Faloona, D. Friesen, S. Haimov, K. Laursen, D. K. Lilly, S. M. Loehrer, Szymon P. Malinowski, B. Morley, M. D. Petters, D. C. Rogers, L. Russell, V. Savic-Jovcic, J. R. Snider, D. Straub, Marcin J. Szumowski, H. Takagi, D. C. Thornton, M. Tschudi, C. Twohy, M. Wetzel, and M. C. van Zanten. Dynamics and chemistry of marine stratocumulus - DYCOMS-II. *Bulletin of the American Meteorological Society*, 84(5):1579−593, 2003.

[10] J.D. Turton and S. Nicholls. A study of the diurnal variation of stratocumulus using a multiple mixed layer model. *The Quarterly Journal of the Royal Meteorological Society*, 113:969−1009, 1987.

[11] S.R. de Roode And J.J. van der Dussen. Large-Eddy Simulati Dussen stratocumulus to cumulus cloud transition as observed during ASTEX. *Boundary-Layers and Turbulence conference, Keystone, CO, USA*, 2010.

# A Poststamp plots

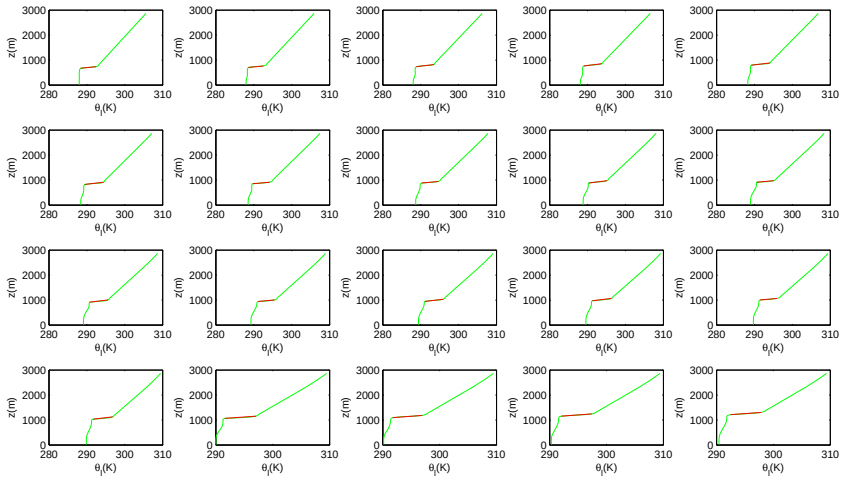


Figure 37: Poststamp plots of $\Delta\theta_l$ for the first 20 hours of the $\Delta\theta_l = 4.5\ K$,$\Delta q_t = -1.1\ g/kg$ case

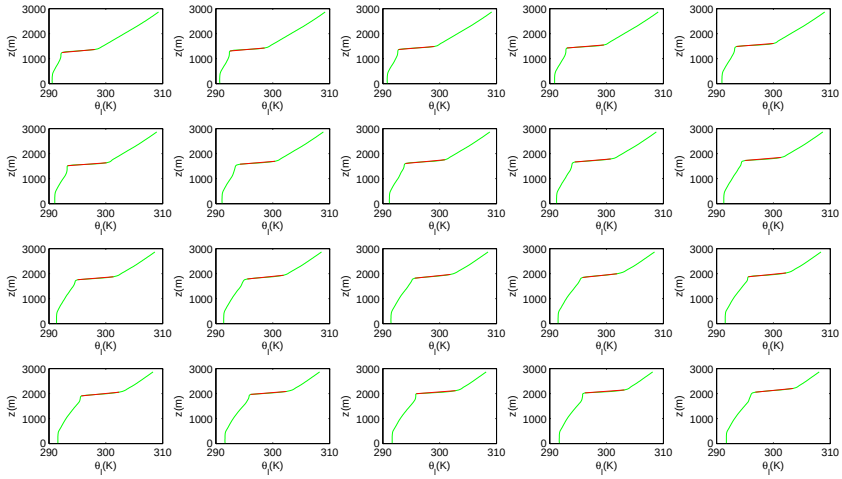


Figure 38: Poststamp plots of $\Delta\theta_l$ for the second 20 hours of the $\Delta\theta_l = 4.5\ K$,$\Delta q_t = -1.1\ g/kg$ case

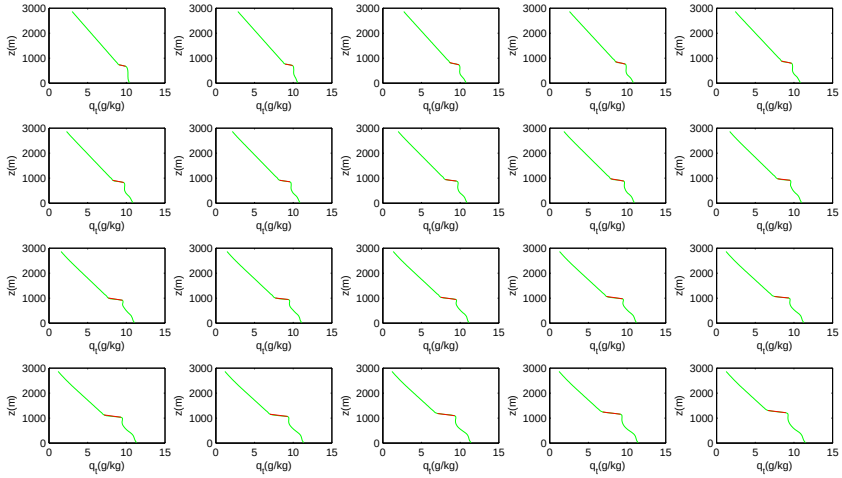


Figure 39: Poststamp plots of $\Delta q_t$ for the first 20 hours of the $\Delta\theta_l = 4.5\ K$,$\Delta q_t = -1.1\ g/kg$ case

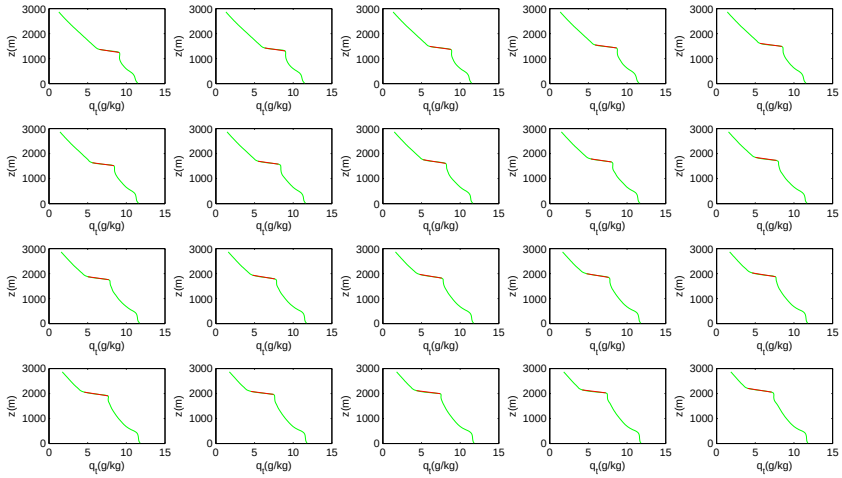


Figure 40: Poststamp plots of $\Delta q_t$ for the second 20 hours of the $\Delta\theta_l = 4.5\ K$,$\Delta q_t = -1.1\ g/kg$ case